

ALMA MATER STUDIORUM · UNIVERSITÀ DI  
BOLOGNA

---

Dipartimento di Fisica e Astronomia “Augusto Righi”  
Corso di Laurea in Fisica

# Facility for $\Lambda_c$ deuteron production in ALICE

Relatore:  
Prof. Andrea Alici

Presentata da:  
Giuseppe Luciano

Correlatore:  
Dott. Nicolò Jacazio

Anno Accademico 2024/2025

---

# Contents

<b>1</b>	<b>Abstract</b>	<b>5</b>
<b>2</b>	<b>Concepts of quantum chromodynamics (QCD)</b>	<b>7</b>
2.0.1	The QCD phase diagram . . . . .	13
2.0.2	The different stage of a heavy-ion collision . . . . .	15
2.0.3	centrality . . . . .	18
<b>3</b>	<b>Thermal model</b>	<b>21</b>
3.0.1	hydrodynamical description . . . . .	21
3.0.2	Anisotropic flow . . . . .	26
3.0.3	Statistical Hadronisation Model (SHM) . . . . .	29
3.0.4	Strangeness and Charmness enhancement . . . . .	32
3.0.5	Computer simulation . . . . .	34
<b>4</b>	<b><math>Y_c N</math> bound state</b>	<b>35</b>
4.0.1	One Boson exchange model . . . . .	35
4.0.2	$\Lambda_c$ N interaction . . . . .	37
4.0.3	Possible $\Lambda_c$ supernuclei . . . . .	41
<b>5</b>	<b>ALICE</b>	<b>45</b>
5.0.1	Inner Tracking System (ITS) . . . . .	47
5.0.2	Time projection chamber (TPC) . . . . .	49
5.0.3	Time Of Flight (TOF) . . . . .	50
5.0.4	Central Barrel Detectors . . . . .	51
5.0.5	Forward Detectors . . . . .	52
5.0.6	Track and vertex reconstruction . . . . .	54
A	Appendix A . . . . .	57
B	Appendice B . . . . .	58
C	Appendice C . . . . .	59

## Ringraziamenti

Un grazie speciale è dedicato a tutti i compagni di viaggio, sia a chi mi è stato vicino nelle interminabili ore sui treni che a quelli che mi hanno accompagnato durante il percorso accademico. I primi che con mirabile genitilezza si

facevano annoiare dai miei racconti ma che erano sempre pronti a ricordarmi che esiste altro oltre a quello che posso vedere coi miei occhi. I secondi invece mi hanno insegnato ad avvicinarmi ad una disciplina tanto affascinante quanto ostica fungendo da inesauribile fonte di ispirazione nel mostrarmi i possibili modi di interfacciarsi ai problemi, ognuno con la propria strategia. Sono stati compagni di interminabili e stravagnati conversazioni dal moto caotico ed imprevedibile, perchè spesso non lo si faceva per il risultato ma più per la genuina voglia di ragionare insieme. Sempre di fretta e sempre senza tempo eppure non si iniziava a lavorare seriamente senza prima aver proposto quell'improbabile argomento che ci bloccava per ore. Grazie ai miei grandi amici su cui ho sempre potuto contare anche se il tempo a loro dedicato non gli ha mai reso giustizia. A tutte quelle volte in cui non potevo uscire e a tutte le volte che mi hanno perdonato perchè se ti presenti con una bottiglia cola sarebbe semplicemente folle continuare a tenere il broncio. Ma infine il pensiero principale è diretto ai miei genitori che anche se tornavo tardi avevano comunque la pazienza di aspettarmi per cena, che mi coccolavano nelle torride giornate di studio estivo con dell'acqua al limone ma nel bicchiere bello perchè anche l'occhio vuole la sua parte, che mi riportavano con i piedi per terra perchè a volte la fantasia ti stacca dal suolo, che a volte il vento non gonfia le vele ma la destinazione è lontana e bisogna remare, che a volte in certe serate persino la luna sembra più vicina ma non ci fai nemmeno caso, e che a volte serve una tesi per capire che non potrò mai ringraziarli abbastanza per tutti i sacrifici che hanno fatto per me.

# Chapter 1

## Abstract

Recent development of hadron spectroscopy revealed that there may exist various molecular bound states of hadrons (observed as hadron resonances). In particular, lot different study, the observation of the unexpected X, Y, and Z mesons and the follow by theoretical studies indicates that heavy quark molecules are more plausible. This can be understood from the balance between the kinetic term and the potential in the Hamiltonian: a heavier system has a smaller kinetic energy. The above naive expectation motivates us to explore possible bound states composed of is, of course, a natural extension of the hypernucleus, which is a nuclear bound state with played a key role in analysing structures of hypernuclei and extracting information on the and it is difficult to perform direct scattering experiments for the hyperons, it is important to get information on their interactions from the three-body or heavier nucleus with strange baryon(s).

There has been an impressive experimental progress in the spectroscopy of heavy hadrons, mainly in the charm sector. The theoretical analysis of hidden and open heavy flavor hadrons has revealed how interesting is the interaction of heavy hadrons, with presumably or resonances in the scattering of two hadrons with heavy flavor content. The observation of events that could be interpreted in terms of the decay of a charmed nucleus [13, 14], fostered conjectures about the possible existence of charm analogs of strange hypernuclei [15–17]. This resulted in several theoretical estimates about the binding energy and the potential-well depth of charmed hypernuclei based on one-boson exchange prospects have reinvigorated studies of the low-energy  $YcN$  interactions



## Chapter 2

# Concepts of quantum chromodynamics (QCD)

Before talking about heavy-ion collision we should introduce some concepts coming from quantum chromodynamics (QCD) and the standard model (SM). The SM describes the universe on the most fundamental level and correctly predicts many of the results of experiment that we have ever done, sometimes with unprecedented levels of accuracy. This theory can explain particles interaction with three different forces: the strong nuclear force, the weak nuclear force, and electromagnetism. The force of gravity is not yet part of the Standard Model but it's straightforward to include it by coupling to a dynamical, curved spacetime [quevedo2024cambridgelecturesstandardmodel]. Fortunately the absence of a quantum gravity theory, that is maybe the most fundamental lack of the SM, is not too influential in the experiment that we can actually perform. In fact physicists believe that the gravity influence will become evident only at the Planck scale. This region may be characterized by particle energies of around  $10^{19}$  GeV or  $10^9$  J on a single particle. The same kinetic energy of a Jumbo jet that travels at  $\approx 250$  km/h. However the SM is very extended and in this thesis we will focus only on the essential aspects for understanding the following chapter.

The QCD is the most successful theory to explain the strong interaction. This force acts on the quarks and is mediated by gluons. The quark is an elementary particle introduced by Gell-Mann and Zweig for understanding the "proliferation of the hadron". In fact, historically, when the energy of the collision starts to increase different particles that interact with the strong force, called hadrons, were discovered. So, to explain the hundred of different hadrons detected, the two scientists proposed that these structures come from different combinations of more fundamental particles, the quark. In particular the name quark comes from the Finnegan's wake, a book of James Joyce, a writer that Gell-Mann loved. Nowadays we know six different types (flavors) of quark usually divided in three generations. The first generation includes quarks up (u) and down (d), the second the quarks strange (s) and charm (c), and the last one

## CHAPTER 2. CONCEPTS OF QUANTUM CHROMODYNAMICS (QCD)

the quark top (t) and bottom (b). A graphical resume of all the particle of the SM is visible in Fig ???. Instead the quantum chromodynamics takes its name because it introduces a property called color charge, the QCD analog of electric charge. First hint about the real existence of color charge was given with the discovery of  $\Delta^{++}$  baryon in 1951. This baryon could be explained only imagining that it is composed of three quark up with the spin aligned. so the configuration of the particle could be written as follows

$$|\Delta^{++}\rangle = |u_{\uparrow}u_{\uparrow}u_{\uparrow}\rangle$$

A highly symmetric configuration. However, since the the particle is a fermion, for the Pauli principle it must have an overall antisymmetric wave function. In 1965, fourteen years after its discovery, this problem was finally understood by the introduction of the charge of colour. With this new parameter we can add another inner space associated to the particle and its configuration can be written as.

$$|\Delta^{++}\rangle = |u_{\uparrow}u_{\uparrow}u_{\uparrow}\rangle \epsilon_{ijk} [C_i \otimes C_j \otimes C_k]$$

where  $\epsilon_{ijk}$  is the Ricci's tensor that permit the wave function to be antisymmetric under quark exchange. Many other strong support of the color charge assumption had been discovered with the passing of time.

Quantum Chromodynamics is based on the gauge group SU(3), the Special Unitary group in 3 (complex) dimensions, whose elements are the set of unitary  $3 \times 3$  matrices with determinant one. Since there are 9 linearly independent unitary complex matrices in three dimension, the condition on the determinant reduced the set at 8 independent directions in this matrix space, corresponding to eight different generators of the group. On a physical level the presence of eight generator predict the existence of eight different gluons. The Lagrangian density of QCD is

$$\mathcal{L} = i\bar{\psi}_q^i \gamma^\mu (D_\mu)_{ij} \psi_q^j - m_q \bar{\psi}_q^i \psi_{iq} - \frac{1}{4} F_{\mu\nu}^a F^{a\mu\nu} \quad (2.1)$$

where  $\psi_q^j$  denotes a quark field with colour index,  $\gamma^\mu$  is a Dirac matrix that expresses the vector nature of the strong interaction, with  $\mu$  being a Lorentz vector index,  $m_q$ , the mass of the quark, allows for the possibility of non-zero quark masses,  $F_{\mu\nu}^a$  is the gluon field strength tensor for a gluon and  $D_\mu$  is the covariant derivative in QCD given by  $(D_\mu)_{ij} = \delta_{ij} \partial_\mu - ig_s t_{ij}^a A_\mu^a$ , with  $g_s$  the strong coupling constant [Skands'2013]. The coupling constant is maybe the most important parameter in defying the properties of the theory, we can imagine it as the probability that a partons, term used for indicate both gluon and quark, of interact in each instant of time whit other partons. The possible vertices of interaction between partons are visible in Fig 2.2. Since this value is considerable during a process the higher order Feynman diagram cannot be neglected and so is particularly difficult to perform analytical calculus. So, as it is said in this cases, the theory is not perturbatively tractable. The



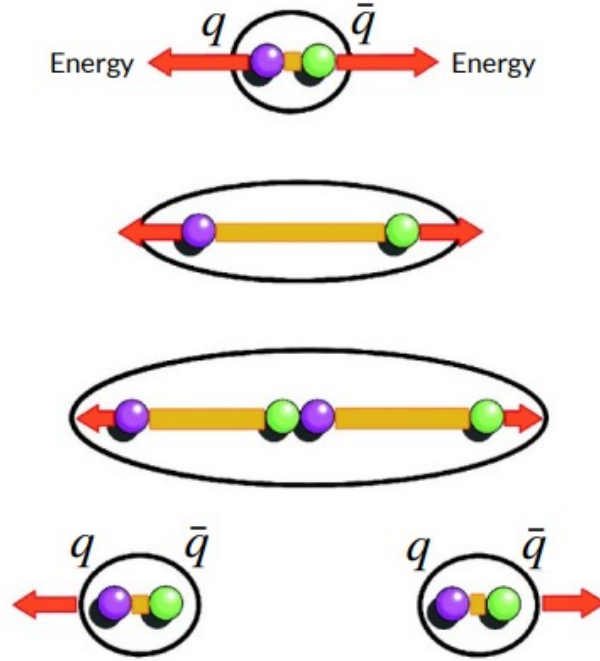


Figure 2.1: The figure resume the process of pair production of quark. ??

QCD exhibit three salient properties: color confinement, asymptotic freedom and the chiral symmetry breaking. Starting from the first one we can say that unlike one may think watching at Eq 2.1 since the gluons are massless the QCD should be a long range force. Instead the common experience tell us that only at very close distances the effect of the interaction are visible. This is possible because the energy for separate the quark grows until a quark-antiquark pair is spontaneously produced, turning the initial hadron into a pair of hadrons instead of isolating a color charge, a graphical resume is visible in Fig 2.1. This is a very efficient way for dissipate the energy and the final result is the production of jets of hadron clearly visible in the experimental data. For these reason the physicist believe that a direct consequence of the theory is the "color confinement" that exclude the possibility of find free quark. However a formal proof had not been yet obtained and this problem has been added to the list of the Millennium Prize Problems.

The asymptotic freedom is a reduction in the strength of interactions between quarks and gluons as the energy scale of those interactions increases. In fact if in a collision the transferred momenta is low we cannot penetrate the cloud of virtual process associated to a particle. Instead, if the transferred momenta increase we can penetrate deeper in the virtual process cloud and so analyze in more detail the "naked particle". The possibility of penetrate deeper in the cloud of virtual process associated to a particle allow us to observe different behaviors of this latter. The asymptotic freedom of QCD was discovered in 1973 by David Gross and Frank Wilczek, [DAVIDPOLITZER1974129].

## CHAPTER 2. CONCEPTS OF QUANTUM CHROMODYNAMICS (QCD)

---

and independently by David Politzer in the same year. For this work, all three shared the 2004 Nobel Prize in Physics. The asymptotic freedom is related to the fact that the quark-antiquark loop has a shielding effect of the color charge and the gluon loop has an anti screening effect. In particular hold that for the coupling constant that.

$$g_s(Q^2) = \frac{g_s(\mu^2)}{1 + g_s(\mu^2) \frac{11n_c - 2n_f}{12\pi} \ln\left(\frac{Q^2}{\mu^2}\right)} = \frac{g_s(\mu^2)}{1 + g_s(\mu^2) \frac{21}{12\pi} \ln\left(\frac{Q^2}{\mu^2}\right)} \quad (2.2)$$

where  $\mu$  is a generic transferred quadri-momenta as  $Q$ ,  $n_f$  is the number of known flavor (assumed six in the SM),  $n_c$  the number of color (assumed three). Is possible to observe that  $11n_c > 2n_f$  and for these reason the anti-shielding effect of the gluon loop is prevalent. From the Eq 2.2 we can desume that the coupling decrease when the transferred momenta increase. the Eq 2.2 is usually expressed showing the scale factor.

$$g_s(Q^2) = \frac{1}{\frac{1}{g_s(\mu^2)} + \frac{21}{12\pi} \ln\left(\frac{Q^2}{\mu^2}\right)} \quad (2.3)$$

defining

$$\frac{1}{g_s(\mu^2)} = \frac{21}{12\pi} \ln\left(\frac{\mu^2}{\Lambda_{CQD}^2}\right) \quad (2.4)$$

$$g_s(Q^2) = \frac{1}{\frac{21}{12\pi} \ln\left(\frac{\mu^2}{\Lambda_{CQD}^2}\right) + \frac{21}{12\pi} \ln\left(\frac{Q^2}{\mu^2}\right)} = \frac{1}{\frac{21}{12\pi} \ln\left(\frac{Q^2}{\Lambda_{CQD}^2}\right)} \quad (2.5)$$

In this way is more evident the point that made the logarithm diverge and the QCD became perturbatively tractable. Experimentally it is found  $\Lambda \sim 200 \div 300$  Mev.[Semprini] With the deployment of computers it has become possible to perform lattice QCD simulations. These simulations can be performed in non-perturbative condition study of the strong interaction by discretizing spacetime into a lattice, which makes it feasible to numerically calculate the behavior of quarks and gluons. Prior to the advent of these advanced computational resources, such detailed simulations were impractical due to the immense complexity involved in solving QCD equations at low energies. However lattice QCD simulations can be very expensive and compromise became indispensable.

In conclusion we can talk about the Chiral symmetry breaking. Massless fermions in Dirac theory are described by left or right-handed spinors. The difference is related to the fact that a particle can have spin either aligned (right-handed chirality), or counter-aligned (left-handed chirality), with his momenta. In the case of massless fermion chirality is a conserved quantum number and the left and right handed spinors can be independently phase transformed. A Dirac mass term explicitly breaks the symmetry but in QCD, the lowest mass quarks are nearly massless and exist an approximate chiral

## CHAPTER 2. CONCEPTS OF QUANTUM CHROMODYNAMICS (QCD)

---

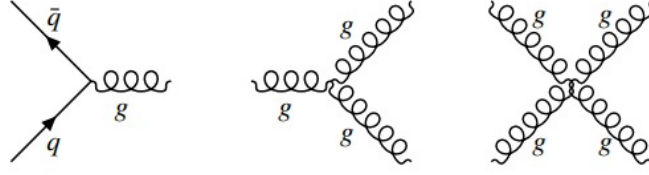


Figure 2.2: The figure show the basilar Feynman diagram of QCD.

symmetry. The vacuum in QCD is non-trivial. It does not simply consist of empty space but it has a rich structure in which quark-antiquark pairs are continually being created and annihilated. This is sometimes referred to as the QCD vacuum. This vacuum is described as a superposition of many states, and the interactions between quarks and gluons cause the system to prefer a certain configuration, which spontaneously breaks the chiral symmetry. The spontaneous symmetry breaking generate masses for hadrons far above the masses of the quarks, and making pseudoscalar mesons exceptionally light. Yoichiro Nambu was awarded the 2008 Nobel Prize in Physics for elucidating the phenomenon in 1960. Lattice simulations have confirmed all his generic predictions. [**Peskin:1995ev**]

For our discussion the Polyakov loop operator gets a particular importance.

$$L = \frac{1}{3} \text{Tr} \left( P e^{ig \int_0^\beta d\tau A_4(\vec{x}, \tau)} \right) \quad (2.6)$$

Where  $P$  is the path-ordering operator and  $A_4$  is the Euclidean temporal component of the gauge field and  $\beta = \frac{1}{T}$  in natural unit,  $T$  temperature. A vanishing thermal expectation value  $\langle L \rangle$  of the Polyakov loop operator thus indicates infinite energy for a free quark, i.e. quark confinement. Studying the equation became evident that as the temperature increases  $\langle L \rangle$  increases rapidly to a nonzero value at high temperatures. This indicates that quark confinement is broken at the corresponding critical temperature  $T_{cr}$ . Experimentally it is found that  $T_{cr} \sim 160$  MeV, which corresponds approximately to  $1.86 \cdot 10^{12}$  K [**Herrmann:2920632**]. We have already discuss that in the absence of quark masses the Eq 2.1 is chirally symmetric. Since the up and down quark masses are very small, neglecting them is a good approximation. The nonvanishing chiral condensate at  $T = 0$  breaks this chiral symmetry and generates a dynamic mass, the so called “constituent” masses. In vacuum this mass are thus about 300 MeV for the up and down quarks, about 450 MeV for the strange quark, 1.5 GeV for the charm, 4.5 GeV for bottom and 180 GeV for top [**Semprini**]. The dynamically generated mass disappeared at  $T_{cr}$ , making the quarks light again and restoring the approximate chiral symmetry of QCD. The dissolution of massive hadrons into almost massless quarks and gluons at  $T_{cr}$  leads to a very rapid rise of the energy density near the deconfinement transition, as shown in Fig 2.3. For a massless gas of quarks and gluons the energy density is proportional to  $T^4$ . We see that for  $T < 4T_{cr}$  the data remain about

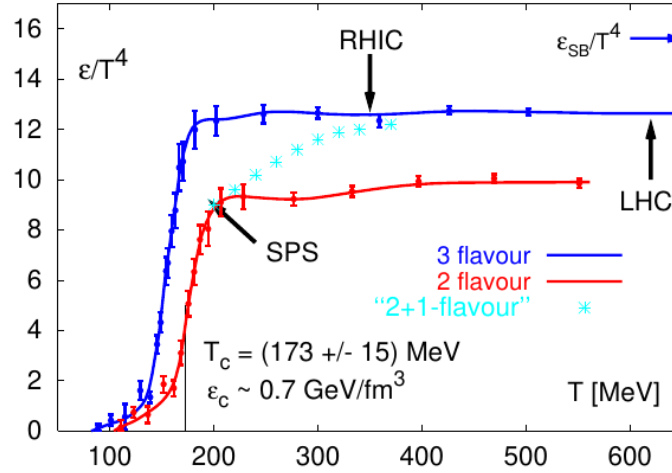


Figure 2.3: The symbol  $\epsilon$  stands for energy density, the curves labelled “2 flavour” and “3 flavor” were calculated for two and three light quark flavors, “2+1 flavour” indicates a calculation for two light and one heavier strange quark flavor.

20% below this Stefan-Boltzmann limit. Instead near  $T_{cr}$  the ratio  $\epsilon/T^4$  drops rapidly by more than a factor 10. This is due to hadronization that we will discuss in the following chapter. The much heavier hadrons are exponentially suppressed below  $T_{cr}$ , leading to a much smaller number of equivalent massless degrees of freedom. According to 2.3 the critical energy density for deconfinement is about  $0.6 \div 0.7 \text{ GeV}/\text{fm}^3$ . However we can have information about the temperature and not directly on the energy density. So the uncertainty of  $\pm 15 \text{ MeV}$  reported in the graph on  $T_{cr}$  introduce a  $\pm 40\%$  uncertainty in the critical energy density, thanks to the  $T^4$  proportional relation, which could be as large as  $1 \text{ GeV}/\text{fm}^3$  or as small as  $500 \text{ MeV}/\text{fm}^3$ . The dependence of  $T^4$  is particularly important because for exceed the critical temperature by only 30% in order to reach the upper edge of the transition region, an energy density  $\epsilon \approx 3.5 \text{ GeV}/\text{fm}^3$  is required and to reach  $2T_{cr}$  the energy density needed arrived at  $23 \text{ GeV}/\text{fm}^3$  [heinz2004conceptsheavyionphysics]. The former number is approximately the value obtained in Pb-Pb collisions at  $\sqrt{s_{NN}} = 17 \text{ GeV}$ . Under the assumption that the total momentum in the region is null we can compute the energy density for colliding nuclei as

$$\langle \epsilon \rangle = 2\rho_0\gamma^2 = \frac{\sqrt{s_{NN}}^2}{2Vmc^2} \quad (2.7)$$

where  $\rho_0$  indicates the energy density at rest of each nucleus and  $\gamma$  is the Lorentz factor of the beam,  $V$  the volume and  $m$  the mass. In heavy ion collision at the Relativistic Heavy Ion Collider (RHIC) for Au-Au collision at  $\sqrt{s_{NN}} = 200 \text{ GeV}$  and  $R \approx 6.98 \text{ fm}$   $\langle \epsilon \rangle = 3 \cdot 10^3 \text{ GeV}/\text{fm}^3$  while for Pb-Pb collision at  $\sqrt{s_{NN}} = 5.02 \text{ TeV}$  and  $R \approx 7.11 \text{ fm}$   $\langle \epsilon \rangle = 2 \cdot 10^6 \text{ GeV}/\text{fm}^3$ , much

## CHAPTER 2. CONCEPTS OF QUANTUM CHROMODYNAMICS (QCD)

---

larger than  $\epsilon_{cr}$  that in the following chapter will assume to be  $\sim 1 \text{ GeV}/fm^3$  for convenience. A more precise formulation of the energy density, valid as long as the particle production exhibits a “plateau” structure in the central rapidity region and the net baryon number at mid-rapidity is close to zero, was given by Bjorken [**PhysRevD.27.140**]

$$\langle \epsilon_B \rangle = \frac{1}{\tau_f \pi R^2} \frac{d\langle E \rangle}{dY} \quad (2.8)$$

Where  $\tau_f$  stands for the formation time of the fireball and  $R$  is the transverse radius of the participant volume for these reason and  $\pi R^2$  is the nuclei overlap area and  $y$  is the rapidity  $y = \frac{1}{2} \ln \frac{E+p_z c}{E-p_z c}$  where  $z$  is the axis in witch the beam is aligned. [**amsdottorato9036**]

### 2.0.1 The QCD phase diagram

Under extreme conditions of density and temperature, hadrons “melt” and release their contents of quarks and gluons. This is possible because at short distances and large momentum transfers the strong interaction, for the already discuss asymptotic freedom, is not so strength for bring together the partons and hadron structures are not possible anymore. Color charges are then deconfined, and this state is called Quark-Gluon Plasma (QGP). For these reason we can consider QGP as the deconfined state of QCD matter and is hottest and most dense liquid known to humankind and, according to the most widely accepted cosmological model, the  $\Lambda$ CDM, were the condition of our universe only few microseconds after the Big Bang.[**QCDPhase-Diagram**]. The ordinary nuclear matter is located at approximately  $T \approx 0 \text{ MeV}$  and  $\mu_B \approx m_N \approx 0.94 \text{ GeV}$  (neutron mass). The baryon chemical potential  $\mu_B$  is a thermodynamic coordinate like the temperature, which can be best understood as the energy required by the system to change its chemical composition. It is tightly connected with the density of quarks: when the former is zero, the latter vanished as well, but we will discuss it better later. If the baryon chemical potential starts to increase, a transition to the QGP state is expected to happen.

In QCD the only viable option to free the hadron constituents is to increase significantly the energy scale of the system by compression or by heating. At this high energy regime hadronic matter melts releasing its elementary degrees of freedom (quark and gluons) in a way which is analogous to a phase transition. A simple description of the phases of nuclear matter is given in Fig 2.4. In order to gain insight into the dynamics of the QCD phase, many studies were performed by using lattice QCD calculations. Particularly problematic is the study of the diagram when  $\mu_B$  approaches 0, like in the condition of the primordial universe. Lattice QCD tells us that even for realistically small up and down quark masses the transition at  $\mu_B = 0$  is most likely not a sharp phase transition but a rapid crossover as shown in Fig 2.4. Recent lattice QCD

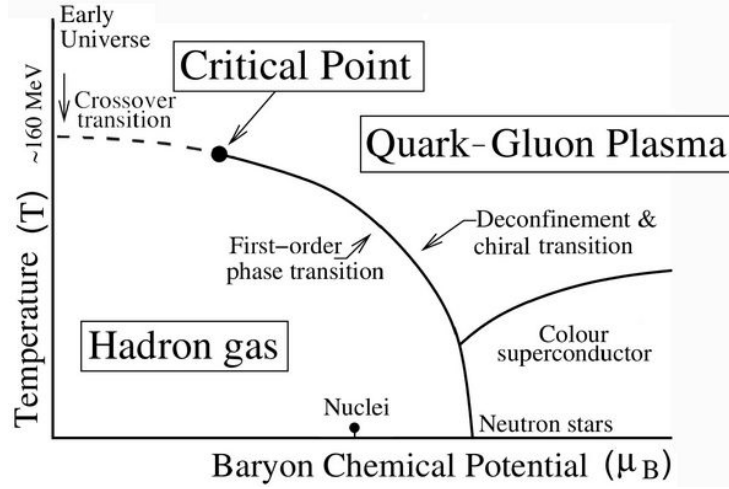


Figure 2.4: A sketched view of the phase diagram of strongly interacting matter, in the plane of temperature and the baryon chemical potential that represents the amount of net baryon charge available in the system [QCDPhase-Diagram]

calculations at moderate non-zero baryon chemical potential indicate that the transition becomes first order at non-zero  $\mu_B$  although the precise value where this happens still remains to be determined by performing calculations with more realistic smaller quark mass. The short line visible in correspondence  $\mu_B = 1$  GeV indicates the nuclear liquid-gas phase transition, with a critical endpoint at a temperature of about 7.5 MeV. At higher temperatures more and more hadron resonances are excited and we have a hadron resonance gas.

At low temperatures and asymptotically large baryon densities quarks are also deconfined, although not in a quark-gluon plasma state but rather in a color superconductor state. In these condition matter carries color charge without loss, analogous to the conventional superconductors that can carry electric charge without loss. The superconducting state is separated from the QGP by a first order transition at a critical temperature estimated to be of order 30-50 MeV. Unfortunately, one cannot use heavy-ion collisions to compress nuclear matter without producing a lot of entropy and therefore also heating it; hence it seems impossible to probe with them the color superconducting phase.

As the center of mass collision energy increases, the colliding nuclei become more and more transparent toward each other. So a decreasing fraction of the beam energy and of the incoming baryons get stopped in the center of mass system. When the energy increase so the incoming net baryons, becoming more and more baryon-antibaryon symmetric making.  $\mu_B$  closer to zero. At the LHC the entropy per baryon ratio  $S/A$  can reach several thousand, still far from the early universe ratio of  $10^9$ , that is, for all practical purposes, “baryon-free” ( $\mu_B = 0$ ) QCD matter. [heinz2004conceptsheavyionphysics].

## 2.0.2 The different stage of a heavy-ion collision

The main stages of relativistic heavy-ion collisions are: Pre-equilibrium, thermalization, hadronization, Chemical freeze-out, and decoupling. This section came from the following article [heinz2004conceptsheavyionphysics], [Herrmann:2920632], [Padhan:2924203], [Arata:2922803] and [amsdottorato9036].

1. **Collision:** At  $t=0$  the collision take place. The nuclei are highly Lorentz contracted, and an extremely dense region of partons is generated with a large energy deposit in the overlap region of the collision. The superposition occur in in  $t_{coll} = 2 \frac{R_N}{\gamma}$ , where  $R_N$  is the nucleus radius. In Pb-Pb collision at  $\sqrt{s_{NN}} = 5.02$  TeV  $t_{coll} \sim 6 \cdot 10^{-3}$  fm/c, smaller than the strong-interaction timescale  $t_{QCD} \sim 1$  fm/c.
2. **Pre-equilibrium** ( $t < 1$  fm/c): The two nuclei just collided. The partons of every participating nucleon interact producing a large amount of quarks and gluons. This process leads to generate high-momentum partons creating jets or heavy quark with the emission of prompt photons. The bulk of the quanta, which are generate from the fraction of the beam energy lost in the collision, create particles with either a large mass or large transverse momenta  $p_{\perp} \gg 1$  GeV/c. The system is now formed by a dense inhomogeneous droplet of strongly interacting QGP matter. In the very early collision stages the momentum transferred is huge and the particle production can be calculated in perturbative QCD. Also if the strong nuclear force is less intense is still the first that manifest it's effect. According to the Heisemberg uncertainty relation the production happens on a time scale  $t \sim \frac{1}{\sqrt[2]{Q^2}}$ , where  $Q$  is the momentum transfers. The key difference between elementary particle and nucleus-nucleus collisions is that the quanta created in the primary collisions between the incoming nucleons can't right away escape into the surrounding vacuum.

In a central collision between two Pb or Au nuclei the nuclear reaction zone has a transverse diameter of about 12 fm, so a hard particle created near the edge and moving towards the center (straight inward) needs about 20 fm/c before it emerges on the other side. During this time the matter thermalizes, expands, cools down and almost reaches decoupling. Moving inside the plasma the particle lose energy. and is possible to proof that the energy loss is proportional to the density of the medium times the scattering cross section between the probe and the medium constituents, integrated along the probe's trajectory. In this way important information about the medium can be analyze. Other probes of the early collision stage are direct photons, either real or virtual, and other process connected to QED such the creation of a couple lepton-antilepton generally known as "dileptons". In contrast

to all hadronic probes, they thus escape from the collision zone without reinteraction and carry pristine information about the momentum distributions of the particle that generated them. Unfortunately, the directly emitted photons and dileptons must be searched in a chaotic background of indirect photons and particles generated in other processes. This renders the measurement of these signals difficult.

3. **Thermalization** ( $t \sim 1 - 15 \text{ fm}/c$ ): The constituents of the fireball frequently interact, establishing a local equilibrium state. The time taken to establish a local thermodynamic equilibrium is called the thermalization time. This phase is characterized by a thermally equilibrated nature that makes the QGP exhibit a perfect fluid behavior and allowing a hydrodynamic description of the medium. This refers to its exceptionally low viscosity, minimal internal friction and high thermal conductivity. Experimental observations, particularly those related to the collective flow of particles produced in heavy-ion collisions, support this behaviour. The produced partons rescatter both elastically and inelastically. Both types of collisions lead to equipartitioning of the deposited energy, but only the inelastic ones change the chemical composition of the medium by changing the flavor of partons. The system, now in equilibrium, builds an internal pressure that finds no opposition by the void that surrounds it. This leads to a rapid hydrodynamic expansion of the system with a decrease in temperature and energy density.
4. **Hadronization** ( $t \sim 20 \text{ fm}/c$ ) As the temperature lowers, the system energy density is not able to keep partons separated and hadrons start to form when the energy density approaches  $\epsilon_{cr}$ . During this phase transition the entropy density drops because of the recombination. However the total entropy cannot decrease. This implies that the fireball volume must increase by a large factor while the temperature remains approximately constant. Since the growth of the fireball volume takes time, the system spends significant time near  $T_{cr}$ . While the matter hadronizes its speed of sound  $v_s = \sqrt{\frac{\partial p}{\partial e}}$  is small causing inefficient acceleration that doesn't permit the collective flow to increase during this phase.
5. **Chemical freeze-out**: When the temperature decreases enough inelastic interactions among hadrons have completely stopped and only the (pseudo-)elastic ones occur. This happens because at this point the matter becomes so dilute that the average distance between hadrons exceeds the range of the strong interactions. The hadrons abundance "freeze out" but the creation of some resonance is however possible but such processes don't change the finally observed chemical composition. Since most of the hadrons in a relativistic fireball are pions, very light



particle  $m_\pi \sim 140$  MeV, resonances with them are very efficient in keeping the system in thermal equilibrium. The chemical freeze-out occurs when  $T = T_{ch}$

6. **Kinetic freeze-out:** At this stage the hadrons, including the then present unstable resonances, start to decouple from the medium as the temperature lowers and the mean free path becomes larger than the mean distance between hadrons. This means that particles are no longer subject to significant interactions and can travel freely to the detector. Now the repartition of the kinetic energy among all hadrons has stopped and the transverse momentum spectrum is approximately exponential. The unstable resonances decay in particle with smaller transverse momenta. Including the consideration on the resonance state is fundamental for explaining completely the originally emitted spectra. Since most resonances decay by emitting a pion, this effect is particularly important for the pion spectrum which at low  $p_\perp$  are completely dominated by decay products. The kinetic freeze-out occurs when  $T = T_{kin} \sim 153$  MeV. The particles then travel towards the ALICE detector, where they are measured at  $t \sim 10^{-15}$  fm/c after the initial collision.

A graphical resume of the process is visible in Fig 2.6 and 2.5

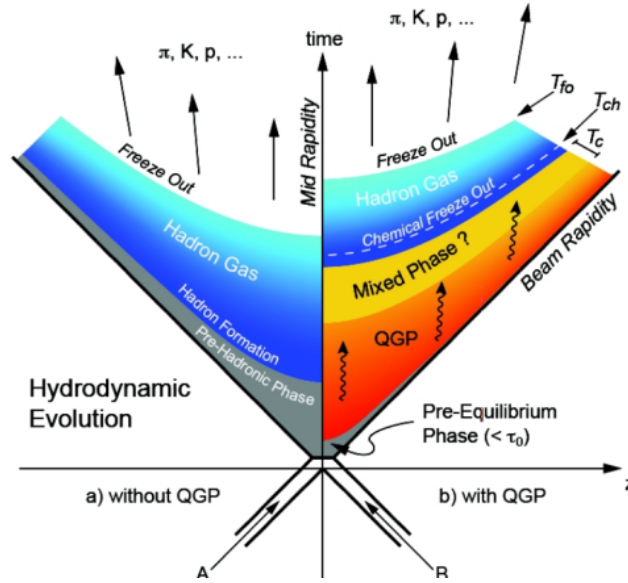


Figure 2.5: Evolution of a central heavy ion collision in a Minkowski-like plane. The two scenarios with and without QGP are pointed out. The critical temperature is indicated by  $T_c$ , while the freeze-out and chemical freeze-out temperatures, are pointed out with  $T_{fo}$ , and  $T_{ch}$ , respectively [Evolution of collisions and QGP].

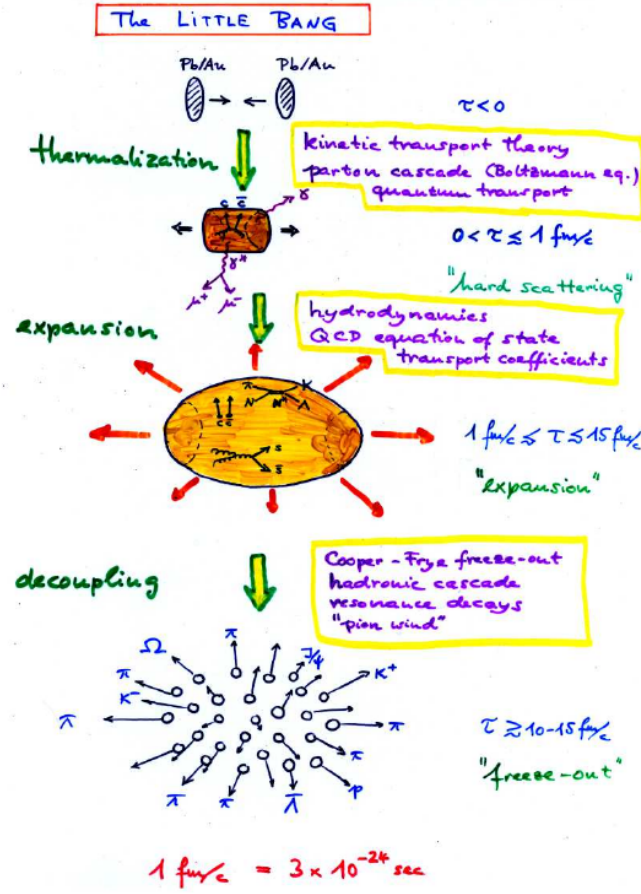


Figure 2.6: A sketched view of the phase of the system after the collision

### 2.0.3 centrality

An important parameter to characterize heavy-ion collisions is the centrality, which is an observable related to the transverse distance ( $\vec{b}$ ) between the centers of the colliding nuclei. The collisions with the smallest  $b$  are called central collisions, and the collisions with large  $b$  are called peripheral collisions. Is expressed in term of the fraction of the total hadronic cross section  $\sigma_{AA}$ . The centrality percentile of collisions with impact parameter ranging in the interval  $[b_1, b_2]$  is given by

$$c(b_1, b_2) = \frac{\int_{b_1}^{b_2} db \frac{d\sigma}{db}}{\int_0^\infty db \frac{d\sigma}{db}} = \frac{\int_{b_1}^{b_2} db \frac{d\sigma}{db}}{\sigma_{AA}} \quad (2.9)$$

The centrality has important consequence in the particle abundances expected, in particular in the number of the charged one. This observable is frequently used and is called multiplicity, defined as the total number of charged particles produced in a collision. For these reason the centrality can be obtain experimentally starting from the measure of the multiplicity or by

## CHAPTER 2. CONCEPTS OF QUANTUM CHROMODYNAMICS (QCD)

---

counting the number of spectator nucleons, the nucleons that non interact during the collision. so if  $N_{ev}$  is the number of collision and  $N_{ch}$  the number of charge particle the centrality can be expressed as

$$c(b_1, b_2) \approx \frac{1}{N_{EV}} \int_{N_{ch-1}}^{N_{ch-2}} dN_{ch} \frac{dN_{ev}}{dN_{ch}} \quad (2.10)$$

$$P(\vec{b}) = \sigma_{NN} T_{AA}(\vec{b}) \quad (2.11)$$

Where  $\sigma_{NN}$  is the cross section and  $T_{AA}$  is the nuclear overlapping function, it can be computed from the single nucleon distribution of the interacting nuclei. It's possible to imagine this parameter as probability to have a nucleon at the same position in the transverse plane in both colliding nuclei. The centrality of each collision has to be determined experimentally in order to identify peculiar behavior that can arise for very specific centrality classes. Only 5% of the total cross section correspond to central interaction. [amsdottorato9036] The centrality can be used to calculate the number of interacting (participant) nucleons  $N_{part}(b)$  and the total number of binary nucleon-nucleon collisions  $N_{coll}(b)$ . The Glauber Model formulation [Miller'2007] assumed that the nucleons are supposed to be point-like and independent, their trajectory is a straight line, the nucleon-nucleon inelastic cross-section does not vary during the collision. All these assumptions go under the name of optical limit. Calling  $A$  and  $B$  the nucleons number respectively in the first and in the second nucleus the probability of having  $n$  nucleon-nucleon interactions is given by the binomial distribution.

$$p(n, \vec{b}) = \binom{AB}{n} \left[ T_{AB}(\vec{b}) \sigma_{innel}^{NN} \right]^n \left[ 1 - T_{AB}(\vec{b}) \sigma_{innel}^{NN} \right]^{AB-n} \quad (2.12)$$

From the mean value of the binomial.

$$\langle N_{coll}(b) \rangle = A B T_{AB}(\vec{b}) \sigma_{innel}^{NN} \quad (2.13)$$

So the number of participant is given by:

$$\begin{aligned} \langle N_{part}(\vec{b}) \rangle = & A \int d^2s T_A(\vec{b}) \left[ 1 - \left( 1 - T_B(\vec{b} - \vec{s}) \sigma_{innel}^{NN} \right)^B \right] \\ & + B \int d^2s T_B(\vec{b} - \vec{s}) \left[ 1 - \left( 1 - T_A(\vec{s}) \sigma_{innel}^{NN} \right)^A \right] \end{aligned} \quad (2.14)$$

With  $T$  the thickness function [Arata:2922803].

## CHAPTER 2. CONCEPTS OF QUANTUM CHROMODYNAMICS (QCD)

---

# Chapter 3

## Thermal model

### 3.0.1 hydrodynamical description

This section resume the information of [heinz2004conceptsheavyionphysics], [phdthesis].

We have already seen that the fireball can be approximately described as an ideal fluid. The approximation hold if the microscopic scattering time scale is much shorter than any macroscopic time scale associated with the fireball evolution. So hydrodynamics becomes applicable when the mean free path of the particles is much smaller than the system size, and allows for a description of the system in terms of macroscopic quantities. For these reason an equation that connect the pressure, the energy density and baryon density i.e. an equation of state is required. Lattice QCD suggest a simplify equation of state for an ideal massless gas.

$$P_{pressure} = \frac{\epsilon}{3} = \frac{d\pi^2 T^4}{90} \quad (3.1)$$

where  $d$  is the effective number of degrees of freedom, value of  $d = 47.5$  for a three flavor QGP which is an order of magnitude larger than that of a pion gas where  $d \sim 3$ . [Snellings'2011]

The possibilities to describe the evolution of the fireball in terms of macroscopic quantities make hydrodynamics the ideal language because it allows ad description of the hadronization phase transition without any need for a microscopic description and at the same time explain the observed collective flow phenomena.

The particles velocities in the fireball are under the effect of pressure gradients and are not independent. For these reason in the final state particle velocities will not be distributed according to random thermal motion, but instead will keep a collective ones. This means that, as happen in an expanding gas, the momentum distribution of particles depend on the position in the plasma and is not completely randomical. This feature is commonly called “collective flow” as opposed to the “non-collective flow” in which particles show uncorrelated velocities. For define the collective flow we can consider

any space-time point in the fireball and considered an infinitesimal volume associate with the point. So the flow velocity can be expressed by  $\vec{v}(x) = \frac{\vec{P}}{P^0}$ , where  $\vec{P}$  is the mean 3-momentum of the particle in the volume and  $P^0$  is the mean energy in quadrivectorial formalism. With  $\vec{v}(x)$  we can associate a normalized velocity  $u^\mu = \gamma(1, \vec{v}(x))$  where  $\gamma$  is the Lorentz factor. In the same manner we can define  $T(x)$  the average local temperature and the  $\mu_i$ , the chemical potential of the  $i$ -th particle species. It's possible to separate the flow velocity into its components along the beam direction ("longitudinal flow"  $\vec{v}_l(x)$ ) and in the plane perpendicular to the beam ("transverse flow"  $\vec{v}_\perp(x)$ ). From now on we use natural unit. In this case the phase-space distribution of particles of type  $i$  is given by the Lorentz covariant local equilibrium distribution.

$$f_{i,eq}(x, p) = \frac{g_i}{e^{(p \cdot u - \mu_i)/T} \pm 1} = g_i \sum_{n=1}^{\infty} (\pm)^n e^{n(p \cdot u - \mu_i)/T} \quad (3.2)$$

Here  $g_i$  is a spin-isospin-color-flavor-etc. degeneracy factor which counts all particles with the same properties. The factor  $p \cdot u$  [<sup>1</sup>] is the energy of the particle in the local rest frame. The  $\pm 1$  in the denominator accounts for the proper quantum statistics of particle (-1 for fermions and +1 for boson). The Boltzmann approximation corresponds to keeping only the first term in the sum in the last expression. In our applications this is an excellent analytical approximation for all hadrons except for the pion because of their mass.

At relativistic energies it is convenient to parametrize the longitudinal flow velocities and momenta in terms of rapidities,  $\eta = \frac{1}{2} \ln \frac{1+v}{1-v}$  in this way  $v = \tanh(\eta)$ . It's also possible to define  $\eta_l = \frac{1}{2} \ln \frac{1+v_l}{1-v_l}$  and  $y = \frac{1}{2} \ln \frac{1+\frac{p_l}{E}}{1-\frac{p_l}{E}} = \frac{1}{2} \ln \frac{E+p_l}{E-p_l}$ . Rapidities have the advantage over longitudinal velocities that they are additive under longitudinal boosts. In fact is possible to express  $\eta_l$  in a given inertial frame which moves relative to the first frame with rapidity  $\Delta\eta$  in the  $-z$  direction has  $\eta'_l = \eta_l + \Delta\eta$ . In addition the previous expression simplified:

$$u^\mu = \gamma_\perp (\cosh \eta_l, v_x, v_y, \sinh \eta_l) \quad (3.3)$$

$$p^\mu = (m_\perp \cosh y, v_x, v_y, m_\perp \sinh y) \quad (3.4)$$

Where  $\gamma_\perp = \frac{1}{\sqrt{1-v_\perp^2}}$  and  $m_\perp = \sqrt{m^2 + p_\perp^2}$  is the transverse mass. For convenience we define also  $\tau = \sqrt{t^2 - z^2}$ , the longitudinal proper time and  $z$  the longitudinal position, and  $\vec{r}_\perp = (x, y)$ .

---

<sup>1</sup>this expression correspond to the quadrivectorial scalar product with the metrical tensor  $P^\mu u_\mu = g_{\mu\nu} P^\mu u^\nu$

$$g_{\mu\nu} = \begin{pmatrix} 1 & 0 & 0 & 0 \\ 0 & -1 & 0 & 0 \\ 0 & 0 & -1 & 0 \\ 0 & 0 & 0 & -1 \end{pmatrix}$$

Bjorken argued that at asymptotically high energies the physics of secondary particle production should be independent of the longitudinal reference frame. Furthermore, the boost-invariance of these initial conditions is preserved in longitudinal proper time if the system expands collectively along the longitudinal direction, in this approximation hold  $\eta = \eta_L$ . For more detail see [PhysRevD.27.140]. The Bjorken scaling approximation is expected to be good at high energies and not too close to the beam and target rapidities. We can so said that

$$p \cdot u(x) = \gamma_{\perp}(\vec{r}_{\perp}, \tau) (m_{\perp} \cosh(y - \eta) - \vec{p}_{\perp} \cdot \vec{v}_{\perp}(\vec{r}_{\perp}, \tau)) \quad (3.5)$$

### The Cooper-Frye formula

In this section we will discuss a formalism for count the total number of particles of species  $i$  produced in the collision. Since this value does not depend on the reference frame of the observer, we must be able to express it in a Lorentz-invariant way. We define a three-dimensional hypersurface  $\Sigma(x)$  in 4-dimensional space-time along which we perform the counting. It's clear that different choices for the hypersurface are possible and the final result must not change as long as it completely closes off the future light cone emerging from the collision point. So for obtaining the count of total particle of each species produced we can study how many particles cross the surface. A possible way for obtain the desired result consist in subdividing it into infinitesimal elements  $d^3\sigma$  and then summing on them. Defining an outward-pointing 4-vector  $d^3\sigma_{\mu}(x)$  perpendicular to  $\Sigma(x)$  at point  $x$  with the magnitude  $d^3\sigma$ . Introducing the 4-vector  $j_i^{\mu}$  describing the current of particles  $i$  through point  $x$ , and summing over all the infinitesimal hypersurface elements we get

$$N_i = \int_{\Sigma} d^3\sigma_{\mu}(x) j_i^{\mu}(x) = \int_{\Sigma} d^3\sigma_{\mu}(x) \left( \frac{1}{(2\pi)^3} \int \frac{d^3p}{E} p^{\mu} f_i(x, p) \right) \quad (3.6)$$

Where  $j_i^{\mu}(x)$  is the particle number current density given in terms of the Lorentz-invariant phase-space distribution. The normal vector can be computed assuming longitudinal boost-invariance, the freeze-out surface can be characterized by a longitudinal proper time. It's possible to proof that

$$d^3\sigma_{\mu} = \left( \cosh \eta, -\frac{\partial \tau_f}{\partial x}, -\frac{\partial \tau_f}{\partial y}, \sinh \eta \right) \tau_f d^2r_{\perp} d\eta \quad (3.7)$$

If the freeze-out surface is  $\Sigma_f = (t_f, x_f, y_f, z_f) = (\tau_f \cosh \eta, \vec{r}_{\perp}, \tau_f \sinh \eta)$  By multiplying the latter parameters with the velocity  $\frac{p^{\mu}}{E}$  and integrating over all momenta with measure  $\frac{d^3p}{(2h\pi)^3} = \frac{d^3p}{(2\pi)^3}$ . We finally obtain the Cooper-Frye formula

$$\boxed{E \frac{dN_i}{d^3p} = \frac{dN_i}{dy p_{\perp} dp_{\perp} d\phi_p} = \frac{dN_i}{dy m_{\perp} dm_{\perp} d\phi_p} = \frac{1}{(2\pi)^3} \int_{\Sigma} p \cdot d^3\sigma_{\mu}(x) f_i(x, p)} \quad (3.8)$$

With  $\phi_p$  is the azimuthal angle. Combing the Eq 3.7 and 3.5 one get

$$p \cdot d^3\sigma_\mu = (m_\perp \cosh(y - \eta) - \vec{p}_\perp \cdot \nabla_\perp \tau_f(\vec{r}_\perp)) \tau_f d^2r_\perp d\eta \quad (3.9)$$

To compute the measured momentum spectrum we can therefore replace the surface  $\Sigma$  by shrinking it to the smallest and earliest surface that still encloses all the processes. We call it the “surface of last scattering” or “freeze-out surface”  $\Sigma_f$ . The the number of particles obtained from the Cooper-Frye formula is not always positive-definite. Physically negative contributions of the Cooper-Frye formula correspond to particles that stream backwards into the hydrodynamical region. It’s possible to compare the negative contribution with the total number particles crossing the transition hypersurface. It is found that the number of underlying inward crossings is much smaller than the one the Cooper-Frye formula gives under the assumption of equilibrium distribution functions. [**Cooper-Frye**]

To compute the measured momentum spectrum the knowledge of the phase-space distribution on the surface of last scattering is required. Since the transition from strong coupling to free-steaming thus happens in a short time interval we may approximate  $f_i(x, p)$  on the last scattering surface. In this section we report only the final momentum distribution obtainable form the Eq 3.8 result but the proof could be find in the appendix A.

$$\begin{aligned} \frac{dN_i}{dy m_\perp dm_\perp} = \frac{g_i}{\pi^2} \int_0^\infty r_\perp dr_\perp n_i(r_\perp) & \left[ m_\perp K_1 \left( \frac{m_\perp \cosh(\rho(r_\perp))}{T(r_\perp)} \right) I_0 \left( \frac{p_\perp \sinh(\rho(r_\perp))}{T(r_\perp)} \right) \right. \\ & \left. - p_\perp \frac{\partial \tau}{\partial r_\perp} K_0 \left( \frac{m_\perp \cosh(\rho(r_\perp))}{T(r_\perp)} \right) I_1 \left( \frac{p_\perp \sinh(\rho(r_\perp))}{T(r_\perp)} \right) \right] \end{aligned} \quad (3.10)$$

Where appear the modified Bessel functions and  $v_\perp = \tanh \rho$ . This formula is useful because it allows to easily perform systematic studies of the influence of the radial profiles of temperature, density and transverse flow on the transverse momentum spectrum, in order to better understand which features of a real dynamical calculation of these profiles control the shape of the observed spectra.

Eq 3.10 can be simplified by assuming instantaneous freeze-out. In this case there is no dependence of the proper time at the freeze-out surface  $\tau$  therefore  $\frac{\partial \tau}{\partial r_\perp} = 0$  so we can rewrite the previous equation in the following manner.

$$\frac{dN_i}{dy m_\perp dm_\perp} = \frac{g_i}{\pi^2} \int_0^\infty r_\perp dr_\perp n_i(r_\perp) \left[ m_\perp K_1 \left( \frac{m_\perp \cosh(\rho(r_\perp))}{T(r_\perp)} \right) I_0 \left( \frac{p_\perp \sinh(\rho(r_\perp))}{T(r_\perp)} \right) \right] \quad (3.11)$$

Commonly named Boltzmann-Gibbs blast wave. This formulation is particularly used for extract properties of the common source such as the temperature  $T_f$  or to fit the single particle spectra. The agreement of Eq 3.11 with the



spectra is quite remarkable especially in central events where the thermal description is expected to work better. However for a more precise description some models take into account also the final state interaction effects, such as the Coulomb repulsion/attraction between charged hadrons which continues long after their strong interactions with each other have ceased.

### Transverse momentum spectra and freeze-out temperature

For all hadrons is observed that  $m_{\perp}/T > 1$  so the modified Bessel function can be approximate in the following manner  $K_{\nu} \sim e^{-\frac{m_{\perp} \cosh \rho}{T}}$ . At  $r_{\perp} = 0$  the radial flow velocity must vanish by symmetry but to larger  $r_{\perp}$  typically rises linearly, it eventually reaches a maximum value and drops again to zero since the dilute tail of the initial density distribution freezes out early. Some simulated profile of grow are shown in the Fig 3.1 [teaney2001hydrodynamicdescriptionheavyion].

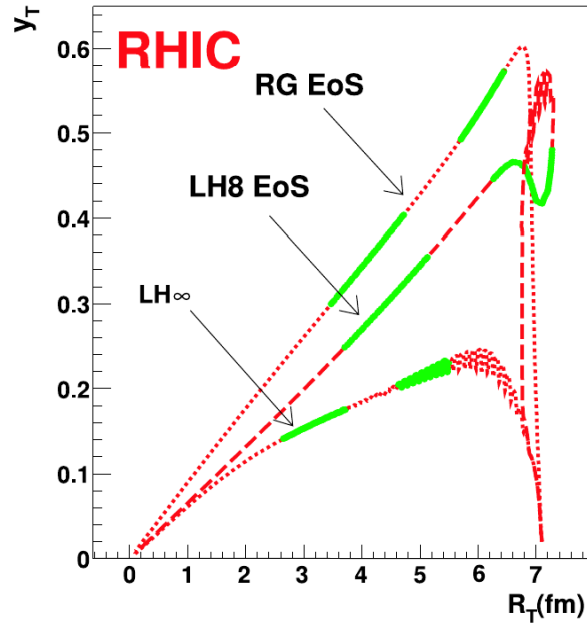


Figure 3.1: Radial flow rapidity profile  $\rho(r_{\perp}) = y_T$  for central Au+Au collisions at RHIC, from hydrodynamic calculations employing three different equations of state [EvolutionofcollisionsandQGP].

Different process can manifest, for example at SPS energies the freeze-out surface moves from the edge inward since the fireball matter cools and freezes out faster than the developing radial flow can push it out. At LHC energies the much stronger radial flow generated by the much higher internal pressure makes the fireball grow considerably arriving at radius of 13 fm/c. For understand how the radial flow influence the spectra first consider the

absence of flow ( $\rho = 0$ ), in this condition  $I_q(0) = 0$  so the Eq 3.10 reduced to

$$\frac{dN_i}{dy m_\perp dm_\perp} \sim m_\perp K_1 \left( \frac{m_\perp}{T} \right) \sim m_\perp^{1/2} e^{-\frac{m_\perp}{T}} \quad (3.12)$$

In these condition as the temperature is the same for all hadron the spectra depend only on the transverse mass, a fact known as " $m_\perp$ " scaling. As visible in the equation the temperature can be extracted easily. Instead if the radial flow is not vanishing approximating  $p_\perp \approx m_\perp$  one get.

$$\frac{dN_i}{dy m_\perp dm_\perp} \sim e^{-\frac{m_\perp (\cosh \rho - \sinh \rho)}{T}} = e^{-\frac{m_\perp}{T_{slope}}} \quad (3.13)$$

With  $T_{slope} = T \sqrt{\frac{1+v_\perp}{1-v_\perp}}$ . Convective flow breaks  $m_\perp$  scaling especially at low  $m_\perp$  as in Fig 3.2. In fact for sufficiently large hadron mass and flow velocity the spectrum develops a blast wave peak at nonzero transverse momentum. In conclusion is possible to summarize these two important limits

$$\text{Non relativistic: } p_\perp \ll m_i \quad T_{i,slope} \approx T_f + \frac{1}{2} m_i \langle v_\perp \rangle^2 \quad (3.14)$$

$$\text{Relativistic: } p_\perp \gg m_i \quad T_{slope} = T \sqrt{\frac{1+v_\perp}{1-v_\perp}} \quad (3.15)$$

This effect are visible in Fig. 3.2 for two flow velocities. These formulations have of course their practical limitations in fact pions, the lightest hadrons, are quickly falling into the relativistic case and few measure are performed at low momenta, especially in collider experiments. In addition, non-relativistic pions are affected by both Bose-Einstein statistics and contribution from resonance decays. Furthermore the  $m_\perp$ -scaling is expected to be more evident for the pp collision while for the heavy-ion case the presence of the radial flow breaks the  $m_\perp$ -scaling. The modification of the spectral shape affects also the mean of the distribution in a mass-dependent way, resulting in an increase of the  $p_\perp$  with the particle mass. This increasing is expected to be more evident when flow is stronger.

### 3.0.2 Anisotropic flow

This section come from [Snellings'2011], [heinz2004conceptsheavyionphysics] [Kolb'2000]. For central collisions between equal spherical nuclei, radial flow is the only possible type of transverse flow allowed by symmetry. In non-central collisions between this azimuthal symmetry is broken and anisotropic transverse flow patterns can develop. The overlap region of the two colliding nuclei is then spatially deformed in the transverse plane. Experimentally, the most direct evidence of flow in the QGP comes from the observation of anisotropic flow which produce anisotropy in particle momentum distributions

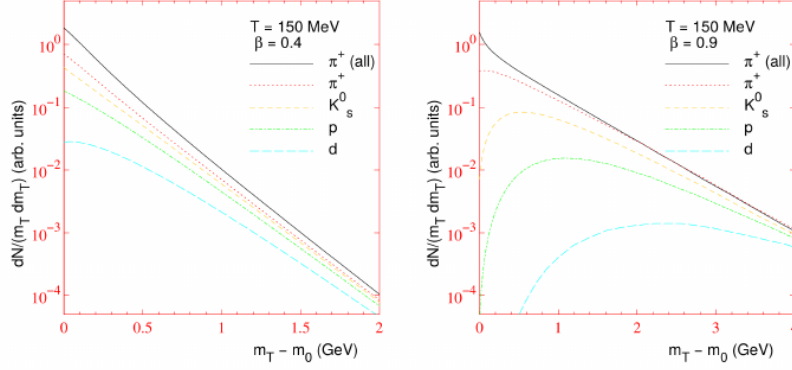


Figure 3.2: Flow spectra for various hadrons as a function of  $m_{\perp} - m_0$  where  $m_0$  is their rest mass. The calculation assumes an infinitesimally thin shell of temperature  $T = 150$  MeV expanding with  $v_{\perp} = 0.9$ . The curve labelled " $\pi^+$  (all)" includes pions from resonance decays in addition to the thermally emitted pions.

correlated with the reaction plane. The evolution of the elliptic shaped interaction volume is shown in Fig 3.4 [kolb2003hydrodynamicdescriptionultrarelativisticheavyion]. The contours indicate the energy density profile and the sequence show time evolution from an almost elliptical region into an almost symmetric system. This expansion happen at the speed of sound already seen. In this situation the equation 3.8 can be written using a Fourier expansion and introducing  $b$ , the impact parameter, and  $\psi_n$  the azimuthal angle of the symmetry plane in the form

$$E \frac{dN_i}{d^3p}(b) = \frac{dN_i}{dy p_{\perp} dp_{\perp} d\phi_p}(b) = \frac{1}{2\pi} \frac{dN_i}{dy p_{\perp} dp_{\perp}}(b) \left( 1 + 2 \sum_{n=1}^{\infty} v_2^i(p_{\perp}, b) \cos(n\phi_p - \psi_n) \right) \quad (3.16)$$

In this Fourier decomposition, the coefficients  $v^1$ ,  $v^2$  and  $v^3$  are known as directed, elliptic and triangular flow respectively. The overlap region of the two colliding nuclei is then spatially deformed in the transverse direction, as visible in Fig 3.3. Is possible to see that the momentum space distribution has a preferred direction. The asymmetry in momentum space can be quantified by the spatial ellipticity:

$$\epsilon_x(b) = \frac{\langle y^2 - x^2 \rangle}{\langle y^2 + x^2 \rangle} \quad (3.17)$$

As a function of time  $\epsilon_x$  decreases, spontaneously due to free-streaming radial expansion (if no rescattering happens) or somewhat more quickly due to the development of elliptic flow (if rescattering occurs) which makes the system expand faster into the reaction plane perpendicular to it. The first mechanism is a consequence of the Heisenberg uncertainty principle because if the definition in the position increase the uncertainty on the linear momentum make the same. Instead the elliptic flow is a consequence of the fact that there is

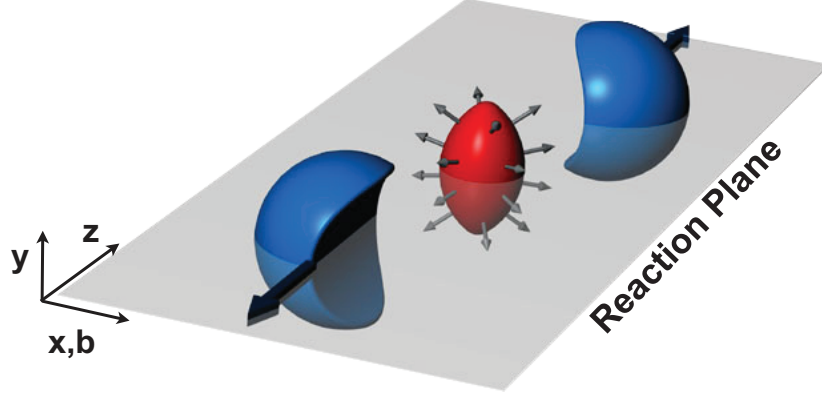


Figure 3.3: Almond shaped interaction volume after a non-central collision of two nuclei. The spatial anisotropy with respect to the x-z plane (reaction plane) translates into a momentum anisotropy of the produced particles (anisotropic flow).

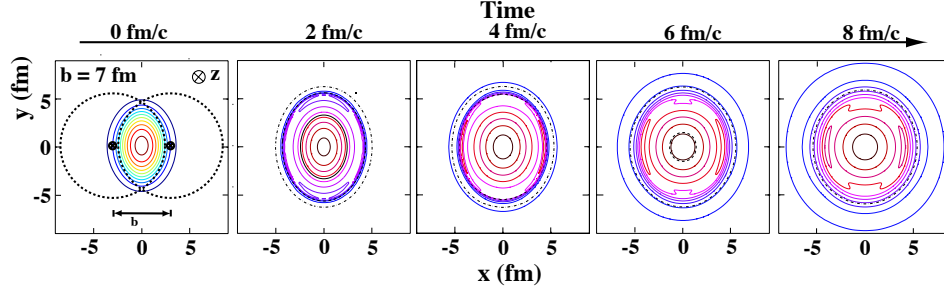


Figure 3.4: The created initial transverse energy density profile and its time dependence in coordinate space for a non-central heavy-ion collision. The z-axis is along the colliding beams, the x-axis is defined by the impact parameter.

high pressure in the interior of the reaction zone which falls off to zero outside. The pressure gradient is very steep in the short direction leading a stronger hydrodynamic acceleration. Hydrodynamics predicts that heavier particles gain more momentum than lighter ones for the previously discussed flattening of their spectra at low transverse kinetic energies. It's possible to show that the spatial eccentricity decrease as a function of time in the following manner, the proof is in the appendix B.

$$\frac{\epsilon_x(\tau_0 + \Delta\tau)}{\epsilon_x(\tau_0)} = \left[ 1 + \frac{(c\Delta\tau)^2}{\langle \vec{r}^2 \rangle_{\tau_0}} \right]^{-1} \quad (3.18)$$

where  $\tau_0$  is the time when the particles were created and  $\langle \vec{r}^2 \rangle_{\tau_0}$  is the azimuthally averaged initial transverse radius squared of the reaction zone. It is also known from microscopic kinetic studies that for a given initial spatial eccentricity the magnitude of the generated elliptic flow is a monotonic function of the mean free path.

More recently, it was realized that small deviations from ideal hydrodynamics, in particular viscous corrections, already modify significantly the buildup of the elliptic flow. The shear viscosity determines how good a fluid is, however, for relativistic fluids the more useful quantity is the shear viscosity over entropy ratio  $\eta_v/s$ . For perfect fluids the ratio can be approximated by:

$$\frac{\eta_v}{s} \approx \frac{\hbar}{4\pi k_B} \quad (3.19)$$

It is argued that the transition from hadrons to quarks and gluons occurs in the vicinity of the minimum in  $\eta_v/s$ , just as is the case for the phase transitions of common life substance like water. The fact that the QGP behaves like an ideal fluid implies strong non-perturbative interactions in the quark-gluon plasma phase.

### 3.0.3 Statistical Hadronisation Model (SHM)

This section had been inspired by the following article [becattini2009introductionstatisticalhadronization] [charm'hierarchy'in'the'statistical'hadronization'model] [heinz2004conceptsheavyionphysics] [amsdottorato9036].

The idea of applying statistical concepts to the problem of multi-particle production in high energy collisions dates back to a work of Fermi in 1950, who assumed that particles originated from an excited region evenly occupying all available phase space states. Note that such a statistical approach has, of course, its limitations. In fact in this way is impossible to investigate correlations between pairs, triplets, quadruplets etc. of particles because they belong to a event and so are not produced entirely independently but correlated in a non-statistical way. For example the momenta of thousand of particle emerging from the fireball must conserve the original momenta of the initially colliding nuclei generating non-statistical momentum correlations among considerably smaller subclusters of particles. So for describe this complex dynamical process, the Statistical Hadronisation Model (SHM) postulates that hadrons are formed from the decay of each cluster in a purely statistical way so. *Every multihadronic state localized within the cluster and compatible with conservation laws is equally likely.*

The volume of the system created in heavy-ion collisions is considerably larger than the partonic scale, this justifies the usage of a grand-canonical ensemble. In particular the volume of clusters is in a constant ratio with their mass when hadronization takes place. Under these conditions the elementary volume under study can exchange both particles and energy with its surroundings. For smaller systems, like happen for example in collision between proton or proton and other nucleus, the grand-canonical ensemble is no longer a good description of the system. In this case the volume created after the collision is considerably smaller and it is better to require the local conservation of quantum numbers and so the canonical formulation is more appropriate. It

is worth noting that the transition from a canonical to a grand-canonical description effectively occurs when the cluster volume is of the order of  $100 \text{ fm}^3$  at an energy density of  $0.5 \text{ GeV}/\text{fm}^3$  [**PhysRevC.65.044901**]. In addition one has to consider the quantum behaviour of both fermionic and bosonic degrees of freedom that form the system. Some possible effect are for example the Bose-Einstein correlations or Hanbury Brown-Twiss interference. The Bose-Einstein correlations refer to a quantum mechanical phenomenon that arises due to the wave-like nature of bosonic particles and their tendency to occupy the same quantum state. Instead the Hanbury Brown and Twiss effect is any of a variety of correlation and anti-correlation effects in the intensities received by two detectors from a beam of particles and depend on the fermionic or bosonic nature of the beam. From statistical mechanics is known that hold

$$\langle N \rangle = \frac{1}{\beta} \left( \frac{\partial \ln Z}{\partial \mu_B} \right) \quad (3.20)$$

$$\langle E \rangle = - \left( \frac{\partial \ln Z}{\partial \beta} \right) + \mu_B \langle N \rangle \quad (3.21)$$

$$\langle S \rangle = k_B \frac{\partial T \cdot \ln Z}{\partial T} \quad (3.22)$$

$$P_{\text{pressure}} = \frac{1}{\beta} \left( \frac{\partial \ln Z}{\partial V} \right) \quad (3.23)$$

Where  $E, S, P_{\text{pressure}}, N, T$  and  $k_B$  are respectively the energy, the entropy, the pressure, the number of particle the temperature and the Boltzmann constant, instead  $\beta = \frac{1}{k_B T}$  and  $Z$  is the partition function that can be expressed in the following manner

$$\ln Z_i(T, V, \mu_i) = \frac{\Delta V g_i}{2\pi^2 \hbar^3} \int_0^\infty \theta_i p^2 dp \ln(1 + \theta_i e^{\beta(\mu_i - E)}) \quad (3.24)$$

$\theta_i$  is +1 for fermions and -1 for bosons. Global observables such as the particle mean multiplicities and entropy can be derived from the previous equation:

$$\langle N \rangle = \frac{\Delta V g_i}{2\pi^2 \hbar^3} \int_0^\infty dp \frac{p^2}{e^{\beta(\mu_i - E)} + \theta_i} \quad (3.25)$$

$$\langle S \rangle = - \sum_i \int_{\Delta V} \int \frac{d^3 x d^3 p}{(2\pi)^3} [f_i \ln f_i + \theta_i (1 - \theta_i f_i) \ln(1 - \theta_i f_i)] \quad (3.26)$$

In this case the distribution is a bit different from the 3.2.

$$f_{i,\text{eq}}(x, p) = \frac{g_i}{e^{\beta(\Delta V)(E_i - \mu_i(\Delta V))} + \theta_i} \quad (3.27)$$

The Eq 3.24 can be further developed the by considering Taylor expansion of the logarithmic part, the full derivation is given in the appendix C.

$$\ln Z_i(T, V, \mu_i) = \frac{\Delta V g_i}{2\pi^2 \hbar^3 \beta} \sum_K \frac{(\theta_i e^{\beta \mu_i})^k}{k^2} m_i^2 K_2(k\beta m_i) \quad (3.28)$$

The definition of the chemical potential  $\mu_i$  is strictly related to the processes at play and to the type of chosen ensemble. It became necessary in order to taking into account the possibility to have fluctuations of the number of particles of species  $i$ . This can happen because the volume, if grand-canonical ensemble, can exchange particles with its surroundings, incrementing or decrementing the components of each species. For a given species  $i$  the chemical potential can be split into  $\mu_i = B_i \mu_B + S_i \mu_S + Q_i \mu_Q$ , where  $B_i$ ,  $S_i$  and  $Q_i$  are respectively the baryon number, strangeness and electric charge while  $\mu_B$ ,  $\mu_S$  and  $\mu_Q$  are the corresponding chemical potentials. If the energy of the collision is not enough the strange quark and antiquark can be non thermalized. So we should add another term to chemical potential, This term take the form  $|s_i| \bar{\mu}_s$  where  $s_i$  is the total number of strange quarks and antiquarks in hadron and  $m \bar{u}_s$  the corresponding potential. However in heavy-ion collisions the  $s$  quarks can be fully thermalized.

Starting from measurements of the identified particle yields ( $dN/dy$ ) in the light flavor sector by using the SHM approach one gains the access to the thermodynamic properties of the system created in the collision. In principle the more particle species are measured the better, in fact all particle that are produced at equilibrium can be used for this purpose. An example of such measurement for different particle species is given in Fig. 3.5. It is possible to see that the large evolution in particle production and identify some key features:

- Particles and antiparticles tend to be equally produced if the collision energy is high enough. This is especially true at LHC energies.
- Baryons ( $p$  and  $\Lambda$ ) and mesons ( $\pi$  and  $K$ ) follow different behaviour with significant baryon/anti-baryon discrepancies at lower energies.
- When  $\mu_B$  is not null the baryonic number of the colliding nuclei is to be found in the products of the collision. Furthermore at low energies a fraction of the initial colliding nucleons are found in the final state (large stopping power). For larger beam energies the colliding nuclei become almost transparent to each other (no baryon stopping) but the original nucleons are less probable to be found.
- At high energies, pions are the most abundant particle species produced
- Particles containing  $s$  or  $c$  quarks are subject to a significant increase in their abundances This effect known as “strangeness enhancement” was

historically identified as a signature typical of the QGP. This aspect will be discussed better later.

- At high energies the production of particles with same mass but different quark content tends to be similar.

The SHM can be used to fit the measured  $dN/dy$  using only a limited number of parameters. This allows to obtain quantities such as the chemical freeze-out temperature, the system volume  $V$  and the chemical potential  $\mu_B$ . Results Fig. 3.6 show how the best fit parameters to describe the data from Pb–Pb central collisions collected by the ALICE experiment at  $\sqrt{s_{NN}} = 2.76$  TeV are:  $T = 156.5 \pm 1.5$  MeV,  $\mu_B = 0.7 \pm 3.8$  MeV,  $V = 5280 \pm 410$  fm<sup>3</sup>. The model is able to describe reasonably well measurements of yields which span over 9 order of magnitudes with a  $\tilde{\chi}^2 = 1.61$  with a low number of free parameters. The largest tension is observed for  $p$  and  $\bar{p}$ , reaching almost a  $3\sigma$  deviation. [Andronic’2017] In addition these results allow for a direct comparison with predictions from lattice QCD. Such comparison is resumed in Fig. 3.7 where it is possible to see that the curve is correctly described.

### 3.0.4 Strangeness and Charmness enhancement

Another success of the SHM model is the prediction of a phenomenon called strangeness enhancement. It consists in an increase in the production of particles that contain strange quarks. In particle production, one would generally expect that the heavier flavours should be suppressed compared to the up and down quarks, both because of their greater mass and the need to preserve quantum numbers. It is known that strong interactions exactly preserve the strangeness quantum number and so the heavier flavours are produced in pairs. Consequently, the production of strange quarks is expected to be suppressed in small collision systems where there is less phase space available for particle production. In fact the creation of a second hadron with a compensating strangeness has to be created inside the same small volume at the same time resulting in a large energetic threshold that the system has to overcome (canonical suppression). Instead the fact that the grand canonical formalism, that assumes only the average conservation of the quantum number, is useful for description of the process tells us that the system behaves as if the strange and antistrange hadrons were created independently and statistically distributed over the entire nuclear fireball. This means that are not important the initial conditions in which the pairs  $s\bar{s}$  are created for determining the final distribution. This point is not completely understood but is probably related to the fact that a significant amount of strangeness diffusion occurs before hadronization.

In heavy-ion collisions, the enhancement of strange hadron production is possible due to the high gluon density of the QGP. This is thanks to the dominance of gluonic production channels, such as the processes  $gg \rightarrow s\bar{s}$ ,



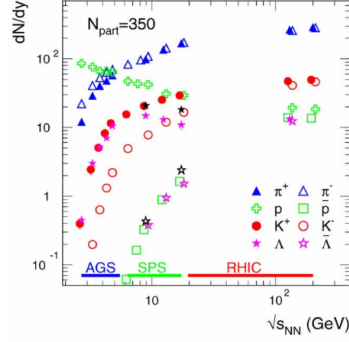


Figure 3.5: The energy dependence of experimental hadron yields at mid-rapidity for various species produced in central nucleus-nucleus collisions. The energy regimes for various accelerators are marked. Note that, for SPS energies, there are two independent measurements available for the  $\Lambda$  hyperon yields. [Andronic'2006]

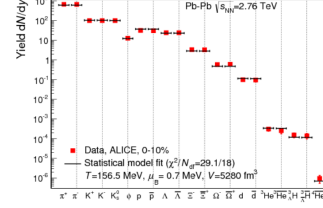


Figure 3.6: adron multiplicities in central (0-10%) Pb-Pb collisions at the LHC, for different particles.[Andronic'2017]

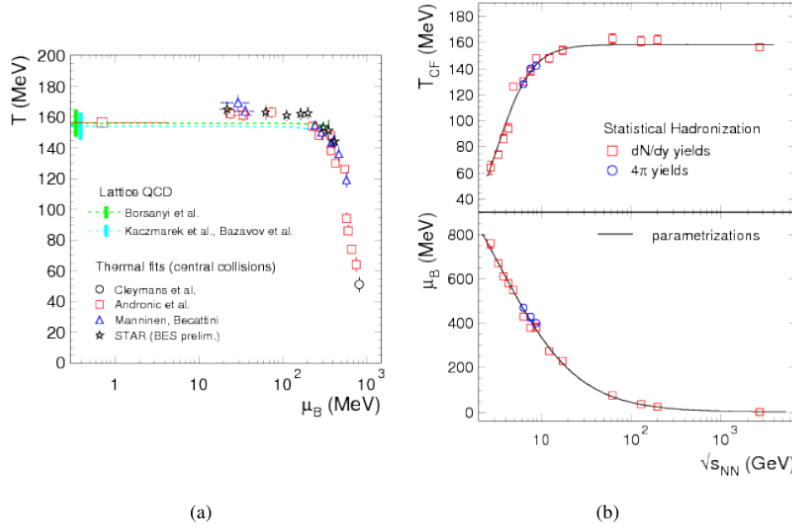


Figure 3.7: The a panel show (a) comparison between the Phase diagram of QCD with data points as obtained at different energies and the thermal model fits from SIS up to LHC data. The panel (b) show the evolution of the temperature of chemical freeze-out and the  $\mu_B$  as a function of the  $\sqrt{s_{NN}}$ . [Andronic'2017]

$u\bar{u} \rightarrow s\bar{s}$  and  $d\bar{d} \rightarrow s\bar{s}$ . In addition, the partial restoration of the chiral symmetry in proximity to the temperature of deconfined transition reduces the constituent mass thus decreasing the energetic threshold for its production. These reduce also the time scale for strangeness saturation that occur for temperatures above 160 MeV. This temperature is close to the one of the chemical freeze-out where the relative particle abundances are fixed. As a consequence when quark-gluon plasma disassembles into hadrons in a breakup process the larger amount of strange quarks available made particle with this quark more abundant in the final state.

Instead the charm quark mass is much larger than the other described in this section and hence thermal production of charm quarks or hadrons is strongly suppressed. However, with increasing center-of-mass energy the total charm production cross section, which results from initial hard collisions, increases strongly. In this case similar considerations made for the strange quark holds also for the heavier charm flavor.

### 3.0.5 Computer simulation

Using an SHM model we have tried to understand how the production of supernuclei is influenced by different parameter. In particular the focus was on the c-deuteron, a bound state of a  $\Lambda_c$  and a neutron. This choice is related to the fact that this nucleons is the easier to observe in heavy-ion collision due to his mass.

# Chapter 4

## $Y_c N$ bound state

### 4.0.1 One Boson exchange model

Before the publication of Hideki Yukawa's groundbreaking papers in 1935 [yukawa], physicists struggled to explain the results of James Chadwick's atomic model, which proposed that protons and neutrons were packed inside a small nucleus with a radius on the order of  $10^{-14} - 10^{-15}$  meters. At such small scales, the electromagnetic forces would be extremely intense, causing the protons to repel each other. In 1932, Werner Heisenberg proposed a "Platzwechsel" (migration) interaction between protons and neutrons within the nucleus, suggesting that neutrons were composite particles made of protons and electrons. According to this model, neutrons would emit electrons, creating an attractive force with protons, and then transform back into protons [heisemerg]. However, this model violated the conservation of linear and angular momentum. To resolve this, Enrico Fermi proposed in 1934 that the emission and absorption of two light particles: the neutrino and electron. A few months later, Soviet physicists Igor Tamm and Dmitri Ivanenko demonstrated that the force associated with the emission of neutrinos and electrons was not strong enough to bind protons and neutrons together in the nucleus.

For these reasons Hideki Yukawa combines both the idea of Heisenberg's short-range force interaction and Fermi's idea of an exchange particle in order to fix the issue of the neutron-proton interaction. For introducing the Yukawa's potential we can start from the Klein-Gordon equation that governs dynamics of free massive scalar, without spin, field

$$\nabla^2 \phi(\vec{r}, t) - \frac{1}{c^2} \frac{\partial^2 \phi(\vec{r}, t)}{\partial t^2} = \frac{m^2 c^2}{\hbar^2} \phi(\vec{r}, t) \quad (4.1)$$

where  $\phi$  is the wave function,  $\vec{r}$  the position,  $t$  the time, and  $m$  the mass of the particle. In spherical coordinate becomes for the radial component.

$$\frac{1}{r^2} \frac{\partial}{\partial r} \left( r^2 \frac{\partial}{\partial r} \phi(\vec{r}, t) \right) - \frac{1}{c^2} \frac{\partial^2 \phi(\vec{r}, t)}{\partial t^2} = \frac{m^2 c^2}{\hbar^2} \phi(\vec{r}, t) \quad (4.2)$$

A solution for the second equation is.

$$\phi(\vec{r}, t) = -g^2 \hbar c \frac{e^{\frac{i}{\hbar}(\vec{r} \cdot \vec{P} - Et)}}{r} \quad (4.3)$$

Where  $\vec{P}$  is the linear momentum and  $E$  the energy. For virtual particles hold that  $0 \sim p^2 c^2 + m^2 c^4$  so  $p \sim \pm i m c$  and with the Einstein-De Broglie equation one get that  $\lambda = \frac{\pm i \hbar}{m c}$ , named Compton wave length, and the solution can be rewritten rejecting the divergent solution as

$$\phi(\vec{r}, t) = -g^2 \hbar c \frac{e^{-\frac{r}{\lambda}}}{r} = -g^2 \hbar c \frac{e^{-\frac{r m c}{\hbar}}}{r} \quad (4.4)$$

The equation 4.4 clarify that massive mediators gives short range interaction. A graphical representation of the phenomena is visible in the Fig 4.1. Yukawa used his equation also to predict the mass of the mediating particle

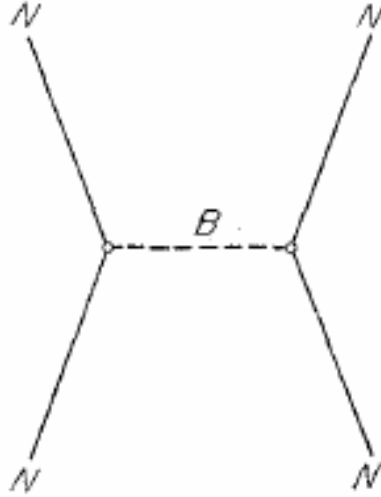


Figure 4.1: The one-boson-exchange diagram of the nucleon-nucleon scattering.

as about 200 times the mass of the electron  $\sim 140$  Mev. Physicists called this particle the "meson," as its mass was in the middle of the leptons and barions. Yukawa's meson was found in 1947, and came to be known as the pion [**Semprini**] The model has been referred to as the "one-boson-exchange model" (OBE model) or the "one-particle-exchange model". This model has presented a new possibility for the realistic understanding of nuclear forces. Basing on the Yukawa potential the Sakata [**sakata**] model was created with the aim of giving a systematic understanding not only of the nucleon-nucleon interaction but of other various strong reactions. While the OBE model is

extremely useful for understanding the basics of nuclear interactions, it has several important limitations that prevent it from being a complete theory of nuclear forces. [**onebosonexchangepotentialmodelapproach**]. Furthermore the theory was expanded and some ideas of the model was included in QCD. However his introduction was important for understand the next section.

### 4.0.2 $\Lambda_c$ N interaction

This section is a resume of the [**Charmed-nucleon**] and [**baryonnucleon-potential**] As we have seen constructing a model for describe, with first-principles analytical calculations, non-perturbative QCD phenomena is very limited. Furthermore the lack of experimental information on the elementary  $Y_c$  N makes the describing of the formation of bound states much more difficult. Thus, the situation can be ameliorated with the use of well constrained models based as much as possible on symmetry principles and analogies with other similar processes. With the notation  $Y_c$  N we mean a bound state of a particle composed by a charm quark, in particular  $\Lambda_c$  and 1, and a nucleon (N).

A model was proposed in the early 1990s in an attempt to obtain a simultaneous description of the light baryon spectrum and the nucleon-nucleon interaction [**Valcarce'2005**]. It was later on generalized to all flavor. In this model, hadrons are described as clusters of three interacting massive (constituent) quarks.

According to Goldstone's theorem, when a continuous symmetry is spontaneously broken, there should be massless particles associated with the broken symmetry. These particles are called Goldstone bosons and can be thought as the excitations of the field in the broken symmetry directions in group space. This spinless boson can acquire a mass if the symmetry is not exact, like in our case, but they typically remain relatively light if compared to other hadrons like protons and neutrons [**Smit'2023**].

Light quarks interact through potentials generated by the exchange of pseudoscalar Goldstone bosons ( $\pi$ ) and their chiral partner ( $\sigma$ ):

$$V_\chi = V_\sigma(r_{ij}^\vec{r}) + V_\pi(r_{ij}^\vec{r}) \quad (4.5)$$

where

$$V_\sigma(r_{ij}^\vec{r}) = \frac{-g_{ch}^2}{4\pi} \frac{\Lambda^2}{\Lambda^2 - m_\sigma^2} m_\sigma \left[ Y(m_\sigma r_{ij} - \frac{\Lambda}{m_\sigma}) Y(\Lambda r_{ij}) \right] \quad (4.6)$$

$$\begin{aligned} V_\pi(r_{ij}^\vec{r}) = & \frac{g_{ch}^2}{4\pi} \frac{m_\pi^2}{12m_i m_j} \frac{\Lambda^2}{\Lambda^2 - m_\pi^2} m_\pi \left[ Y(m_\pi r_{ij} - \frac{\Lambda^3}{m_\pi^3}) Y(\Lambda r_{ij}) \right] \vec{\sigma}_i \cdot \vec{\sigma}_j \\ & + \left[ H(m_\pi r_{ij}) - \frac{\Lambda^3}{m_\pi^3} H(\Lambda r_{ij}) \right] S_{ij}^2(\vec{\tau}_i \cdot \vec{\tau}_j) \end{aligned} \quad (4.7)$$

$\frac{g_{ch}^2}{4\pi}$  is the chiral coupling constant,  $m_i$  are the masses of the constituent quarks,  $\Lambda \sim \Lambda_{CSB}$ ,  $Y(x) = \frac{e^{-x}}{x}$  is the standard Yukawa function,  $H(x) = (1 + \frac{3}{x} + \frac{3}{x^2})Y(x)$ ,  $S_{ij} = 3(\vec{\sigma}_i \cdot \hat{r}_{ij})(\vec{\sigma}_j \cdot \hat{r}_{ij})\vec{\sigma}_i \cdot \vec{\sigma}_j$  is the quark tensor operator. Instead perturbative QCD effects are taken into account through the one-gluon-exchange (OGE) potential

$$V_{OGE}(\vec{r}_{ij}) = \frac{\alpha_s}{4} \vec{\lambda}_i^c \cdot \vec{\lambda}_j^c \left[ \frac{1}{r_{ij}} - \frac{1}{4} \left( \frac{1}{2m_i^2} + \frac{1}{2m_j^2} + \frac{2\vec{\sigma}_i \cdot \vec{\sigma}_j}{3m_i m_j} \right) \frac{e^{-r_{ij}/r_0}}{r_0^2 r_{ij}} \frac{3S_{ij}}{4m_i m_j r_{ij}^3} \right] \quad (4.8)$$

where  $\vec{c}$  are the SU(3) color matrices,  $r_0 = \hat{r}_0/\nu$  is a flavor-dependent regularization scaling with the reduced mass  $\nu$  of the interacting pair, and  $\alpha_s$  is the scale-dependent strong coupling constant given by:

$$\alpha_s(\nu) = \frac{\alpha_0}{\ln[(\nu^2 + \mu_0^2)/\gamma_0^2]} \quad (4.9)$$

$\alpha_0=2.118$ ,  $\mu_0 = 36.976$  Mev and  $\gamma_0=0.113$  fm<sup>-1</sup>. the equation 4.9 give rise  $\alpha_s \sim 0.54$  for light quark and  $\alpha_s \sim 0.43$  for uc pairs. The table resume all the parameter 4.1

$m_{u,d}$ (MeV)	313	$g_{ch}^2/4\pi$	0.54
$m_c$ (MeV)	1752	$m_\sigma$ (fm <sup>-1</sup> )	3.42
$\hat{r}_0$ (MeV fm)	28.170	$m_\pi$ (fm <sup>-1</sup> )	0.70
$\mu_c$ (fm <sup>-1</sup> )	0.70	$\Lambda$ (fm <sup>-1</sup> )	4.2
$b$ (fm)	0.518	$a_c$ (MeV)	230

Table 4.1: The table summarizes the typical values of the parameters present in the previous equation.

Finally, any model imitating QCD should incorporate confinement. Although it is a very important term from the spectroscopic point of view but it is negligible for the hadron-hadron interaction. Lattice QCD calculations suggest a screening effect on the potential when increasing the interquark distance which is modeled here by.

$$V_{CON}(\vec{r}_{ij}) = -\alpha_c(1 - e^{-\mu_c r_{ij}})\vec{\lambda}_i^c \cdot \vec{\lambda}_j^c \quad (4.10)$$

The figures 4.1 shows the different diagrams contributing to the charmed baryon-nucleon interaction. The first type of interaction, visible in (a) and (b), is mediated by the exchange of a boson between light quark or between a light and heavy flavor. The second one instead take in account also the exchange of the identical light quark (c) and (d). The second possibility correspond to short range that contain one-gluon exchange contributions not present in normal interaction in ordinary nucleus. In the limit where the two baryons  $Y_c N$  overlap, the Pauli principle impose antisymmetry requirements. Such

effects, if any, will be prominent for relative S waves ( $L = 0$ ). The S wave normalization kernel of the two-baryon wave function can be written in the overlapping region ( $R \rightarrow 0$ )

$$N \rightarrow 4\pi \left[ 1 - \frac{R^2}{8} \left( \frac{5}{b^2} + \frac{1}{b_c^2} \right) [1 - 3C(S, I) + \dots] \right] \quad (4.11)$$

Where  $C(S, I)$  is a spin-isospin coefficient and  $b, b_c$  are the Gaussian parameters for the wave function of the light and charmed quarks, respectively, assumed different for the sake of generality. This normalization of the wave function at short distances, generating Pauli repulsion. The repulsion occurs when  $C(S, I) = 1/3$ , there might exist Pauli suppressed channels.

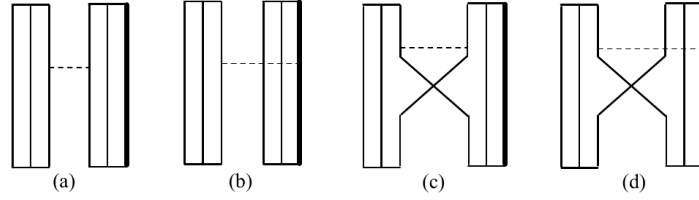


Figure 4.2: The vertical solid lines represent a light quark,  $u$  or  $d$ . The vertical thick solid lines represent the charm quark. The dotted horizontal lines stand for the exchanged boson. (a) Interaction between two light quarks. (b) Interaction between the heavy and a light quark. (c) Interaction between two light quarks together with the exchange of identical light quarks. (d) Interaction between the heavy and a light quark together with the exchange of identical light quarks.

A numerical simulation of the potential is described in [MIYAMOTO2018113] performed with lattice QCD with lattice spacing  $a = 0.0907(13)\text{fm}$  and a physical lattice size of  $L a = 2.902(42)\text{fm}$ . The figure 4.3 shows the  $\Lambda_c N$  central potential in the  $^1S_0$  channel for each ensemble with different mass considered for the pion. For Ensemble 1  $m_\pi \sim 700\text{ MeV}$ ,  $m_\pi \sim 570\text{ MeV}$  for Ensemble 2 and  $410\text{ MeV}$  for Ensemble 3. They found a repulsive core at short distances ( $r \lesssim 0.5\text{ fm}$ ) and an attractive one for intermediate distances ( $0.5 \lesssim r \lesssim 1.5\text{ fm}$ ). The same calculation has also been performed with a  $\Lambda_c N$  system with  $J^P = 1^+$  obtaining the result visible in figure 4.4. The two results are qualitatively and quantitatively similar except at short distance ( $r \lesssim 0.5\text{ fm}$ ). As can be seen there is a tendency that the attraction obtained by the latest lattice QCD simulations for both  $\Lambda_c N$  S waves becomes stronger as the pion mass decreases, moving towards the predictions of the CQM. However the  $^3S_1$  potential is more attractive than  $^1S_0$ . This is due to the short-range dynamics consequence of gluon and quark exchange. If no meson exchanges were considered, the S wave phase shifts of the  $\Lambda_c N$  system are very similar to the corresponding NN scattering. In both partial waves one obtains typical hard-core phase shifts due to the short-range gluon and quark-exchange dynamics. However, the hard-core radius in

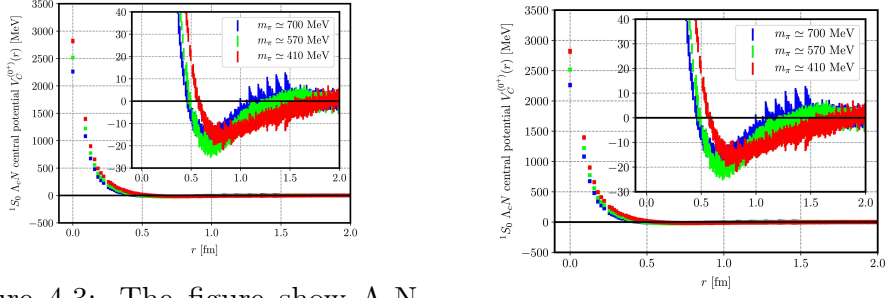


Figure 4.3: The figure show  $\Lambda_c N$  central potential in the  $1S_0$  channel for each ensemble. The potential is calculated for  $m_\pi \approx 700$  MeV case (Blue), for  $m_\pi \approx 570$  MeV case (Green) and for  $m_\pi \approx 410$  MeV case (Red). Figure 4.4: The figure show  $\Lambda_c N$  central potential in the  $3S_0$  channel for each ensemble. The potential is calculated for  $m_\pi \approx 700$  MeV case (Blue), for  $m_\pi \approx 570$  MeV case (Green) and for  $m_\pi \approx 410$  MeV case (Red).

the spin-singlet state is larger than in the spin-triplet one leading to a more attractive interaction in the spin-triplet partial wave due to a lower short-range repulsion. In fact, the hard cores caused by the color magnetic part of the OGE potential have been calculated obtaining 0.35 fm for the spin-triplet state and 0.44 fm for the spin-singlet one.

Few years ago [**PhysRevC.99.045208**] the following study has presented a charmed baryonnucleon potential based on a SU(4) extension of the meson-exchange potential. The study has analyze different models of the interaction which differ only on the values of the couplings of  $\sigma$  meson with the charmed baryons. In a first model the couplings of the  $\sigma$  meson with the charmed baryons are assumed to be equal to those of the  $\Lambda$  and  $\Sigma$  hyperons for make comparison with the data and other model. Then these couplings were reduced by 15% and 20% respectively. The  $\Lambda_c N$  phase shifts obtained with these models are in qualitative agreement with the CQM results. However they predict a higher overall attraction for the  $^3S_1$  than for the  $^1S_0$  supporting the previous observation.

The weaker potential than  $\Lambda_c N$  could be explained from following facts:

- The long-range contribution is expected to be caused by the K meson exchange for  $\Lambda N$  interaction. In the system, however, the K meson (strange quark) exchange is replaced by the D meson (charm quark) exchange, and this contribution is highly suppressed due to the much heavier D meson mass than the K meson mass.
- The one-pion exchange in the  $\Lambda N - \Sigma N$  transition is considered to give a contribution to the effective  $\Lambda N$  interaction. Instead this contribution is expected to be suppressed due to the large mass difference between  $\Lambda_c N$  and  $\Sigma_c N$



### 4.0.3 Possible $\Lambda_c$ supernuclei

One of the most interesting applications of the charmed baryon-nucleon interaction is the study of the possible existence of charmed hypernuclei. Since the  $\Lambda_c$  interaction is dominated by the spin-independent central force, as we discussed in the previous section, the spectrum of hypernuclei, if they exist, would probably can be approximated by the following single-folding potential defined by

$$V_f(\vec{r}) = \int d^3f' \rho_A(\vec{r}') V_{\Lambda_c N}(\vec{r} - \vec{r}') \quad (4.12)$$

where  $\rho_A(\vec{r})$  correspond to ne nuclear density corresponding with the atomic number A and  $V_{\Lambda_c N}$  stands for the two body spin-independent central potential of the  $\Lambda_c$  system. The study described assumed,

$$\rho_A(\vec{r}) = \rho_0 \left[ 1 + e^{\frac{r-c}{a}} \right] \quad (4.13)$$

where the parameters employed  $\rho_0$ , c, a are the same used for described spherical nuclei. They test the equation with different set of parameter taking the value assumed in the following nuclei  $12^C$ ,  $28^Si$ ,  $40^Ca$ ,  $58^Ni$  and  $208^Pb$ . With the following potential they calculate the binding energy for  $\Lambda_c$  hypernuclei by the Gaussian expansion method. The result is shown in figure 4.5. As expected the binding increases as the atomic number increases. Furthermore, as the potential approaches to the physical one (as the u, d quark masses decrease toward physical values), the binding energy increases. These results suggest that hypernuclei may exist, if their binding energy is larger than the Coulomb repulsion energy described by??.

binding energies of the  $Y_c N$  two-body systems as a function of the boson-exchange The binding energies of the  $J P = 1+$  state are always a little bit larger than those of the  $J P = 0+$  state. This is due to the similar contribution of the boson-exchange potentials in both partial waves, the difference coming from the channel coupling that enhances the D wave probability. Thus, while for  $\mu = 1.2$  GeV the probability of the  $1 S0$  cN channel in the  $J P = 0+$  state is 98.2% the  $1 S0$  channel in the  $J P = 1+$  state is 97.6% difference between the  $1 S0$  and  $3 S1$  probabilities in the  $J P = 0+$  and  $1+$  states, remains almost constant for any value of  $\mu$ . For example, for  $\mu = 1.6$  GeV they are 80.179.61.8 to 10.1% the  $J P = 0+$  state. As can be seen, the uncoupled  $1 S0$  cN state is bound for any value of the cutoff

It's interesting to confront energy expectation taking into account also the Coulomb repulsion, the result is reported in figure 4.6. It's possible to see that only the system with lower atomic number could eventually exist.

On the one hand, it would be favored, bearing in mind the tendency that the c N attraction becomes stronger as the pion mass decreases. On the other hand, since the average cN (N) potential that it is relevant for the charmed hypertriton (hypertriton) is dominated by the spin-singlet channel [57], the considerably smaller  $1 S0$  cN scattering length compared to the N system goes

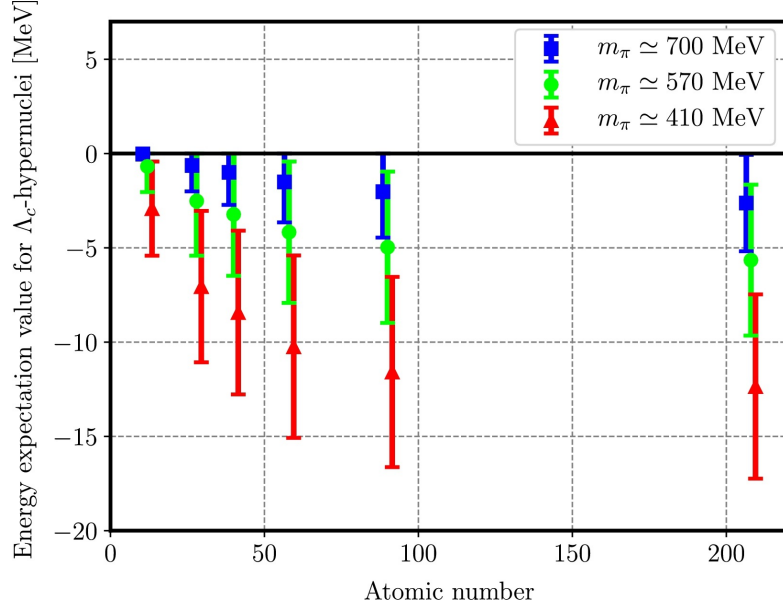


Figure 4.5: The figure show the binding energy in symmetric nuclei with the parameter assumed for each atomic number for each ensemble. The binding energies are calculated from the folding potentials for  $\Lambda_c$  hypernuclei by using the Gaussian expansion method. The folding potentials are constructed from the spin-independent central potential of the  $\Lambda_c N$  system

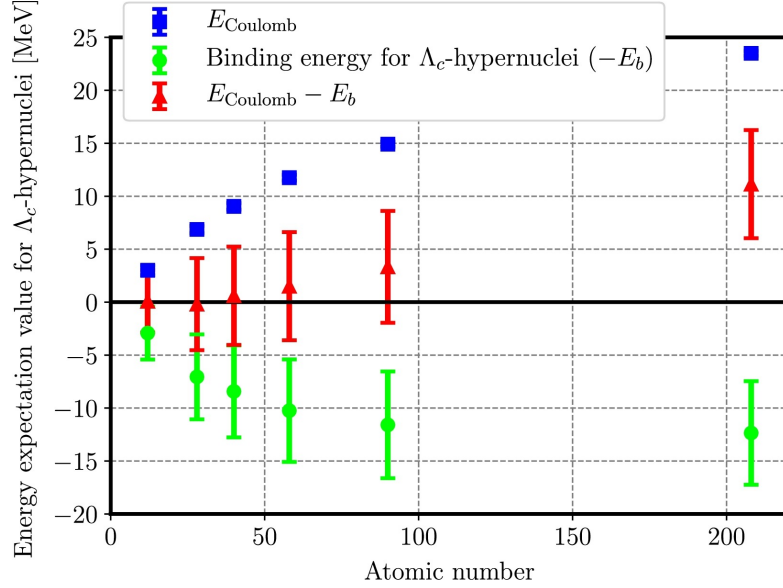


Figure 4.6: The figure show the expectation value of folding potential for Coulomb force in  $\Lambda_c$  hypernuclei (Blue). The expectation values are calculated from the binding solution of the  $\Lambda_c$  hypernuclei for Ensemble 3 ( $m_\pi \approx 410$  MeV). For comparison, the binding energy of  $\Lambda_c$  hypernuclei (Green) and sum of them (Red) are also plotted.

against its existence. The balance could be tilted if the spin dependence of the  $c$   $N$  interaction induced by the short-range dynamics would slightly enhance the attraction in the spin-triplet partial wave as compared with the spin-singlet one. Then, the existence of  $J = 3/2$   $c$  hypernuclei might be considered seriously. The isoscalar  $J = 3/2$  state is dominated by the more attractive spin-triplet interaction [58], which together with the reduction of the kinetic energy associated with the  $c$  induced by its larger mass as compared to the  $\Lambda$ , could lead to a slightly bound  $J = 3/2$   $c$  hypernucleus [

The binding energy of  $\Lambda_c$  hypernuclei has been analyzed in ?? using the HAL QCD for  $m_\pi = 410$  MeV.



# Chapter 5

## ALICE

The A Large Ion Collider Experiment (ALICE) is a detector designed for heavy-ion physics at the Large Hadron Collider (LHC). It is primarily used to study lead-lead collisions, recreating conditions similar to those just after the Big Bang. These extreme conditions may also be present in neutron stars and other astrophysical objects. The goal of ALICE is to recreate and study quark-gluon plasma. This is crucial for the understanding of the formation and evolution of quark-gluon plasma, the mechanisms that confine quarks and gluons, and the nature of the strong nuclear force. This force plays a key role in generating the bulk of the mass of ordinary matter. ALICE also investigates phenomena such as quark confinement and chiral symmetry restoration, which are important for understanding the fundamental behavior of matter at the smallest scales. The ALICE collaboration uses the 10 000-tonne ALICE detector 26 m long, 16 m high, and 16 m wide to study quark-gluon plasma. The detector sits in a vast cavern 56 m below ground close to the village of St Genis-Pouilly in France, receiving beams from the LHC. [Alice] The lead isotope used in LHC is  $^{208}\text{Pb}$ . The lead is taken from lead vapor obtained heating the substance and then with a electrons are stripped with electric current. A sketch of the ALICE coordinate system is shown in Fig ?? In this figure, the (x, y, z) axes are shown together with the spherical coordinates used to describe the trajectory of particles in ALICE, (r,  $\theta$ ,  $\psi$ ).

The ALICE sub-detectors are categorized into three main groups: one at mid-rapidity  $|\eta| \leq 1$ , the central barrel, and one at forward rapidity  $-4 < \eta < -2.5$ , and the the muon spectrometer dedicated to muon identification. However the muon spectrometer is included in the forward detectors. The apparatus scheme can be resumed in the following manner.

- The central barrel detectors can measure all over the azimuthal angle and include in order from the interaction point and going outward:
  1. The Inner Tracking System (ITS) is a silicon tracking system composed of six cylindrical layers. its main goal is to identify the position of the primary vertex with a resolution better than 100

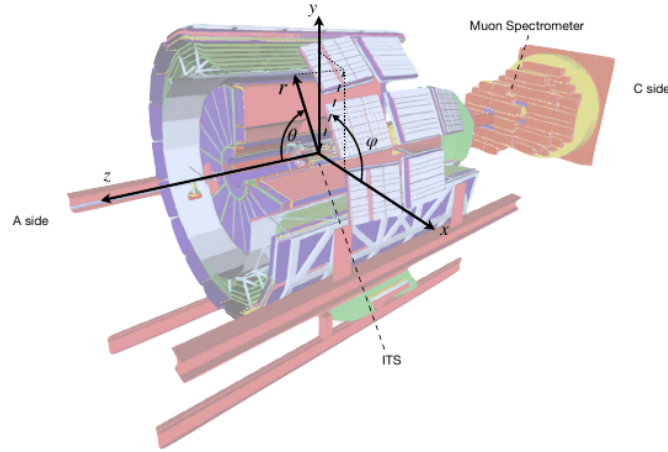


Figure 5.1: The figure show the cylindrical coordinate set used for describe the position of the object with respect the cartesian one [Herrmann:2920632].

$\mu\text{m}$  and provide tracking of charged particles. of charged particles down to

2. the Time Projection Chamber (TPC) is used for charged particle identification.
3. the Transition Radiation Detector (TRD) is composed of different gas chamber and radiation for identify and track electrons
4. the Time of Flight (TOF) measure the time of flight providing important information for particle identification and a dedicated trigger for cosmic ray events and Ultra Peripheral Collision collisions (UPC).

These subsystem are mostly dedicated to vertex reconstruction, tracking, particle identification and momentum measurement. Are also present some specialized detectors with limited acceptance.

1. High-Momentum Particle Identification Detector (HMPID) is used for study Cherenkov photons for identify particle with  $p_{\perp} \gtrsim 1 \text{ GeV}/c$
2. PHOTon Spectrometer (PHOS), is an electromagnetic calorimeter used for photons identification and as high-energy photon trigger.
3. ElectroMagnetic CaLorimeter (EMCal) is a Pb-scintillator calorimeter for identify photons and pion with  $\eta \lesssim 0.7$  and is also used as jet trigger.
4. Di-jet Calorimeter (DCal).

- The forward detector include:

1. Muon spectrometer for reconstruct heavy quark hadrons through their weak decay in the channel  $\mu^- \bar{\nu}_\mu$  or  $\mu^+ \nu_\mu$  or for electrodynamic decay in the couple  $\mu^+ \mu^-$
2. Forward Multiplicity Detector (FMD) composed by several layers of silicon strip detectors at a distance of 70÷150 cm from the interaction point.
3. Photon Multiplicity Detector (PMD)
4. Zero Degree Calorimeters (ZDC) a proton and neutron calorimeter
5. V0 Detectors
6. T0 detectors

[Padhan:2924203] [Arata:2922803]

In the following section we will discuss some of the most important one. A graphical resume is visible in Fig 5.2

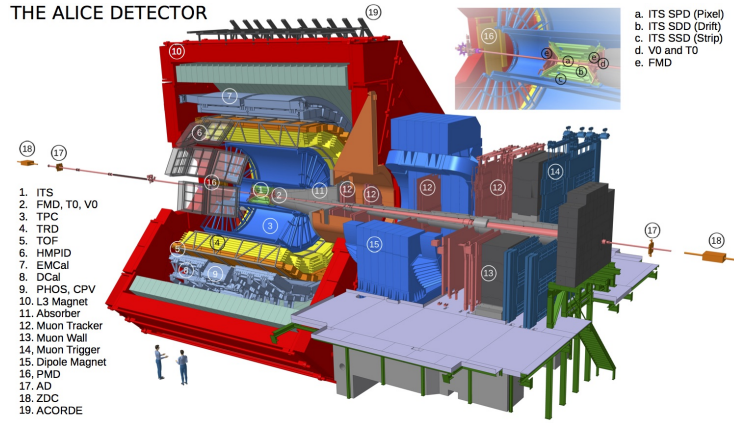


Figure 5.2: The figure show the Layout of the ALICE detector in Run2 with their position and dimension [Botta:2017bwj]

### 5.0.1 Inner Tracking System (ITS)

The Inner Tracking System (ITS) is a crucial part of the ALICE tracking system, positioned as the innermost sub-detector of the central barrel, closest to the beam pipe and the interaction point. It consists of six concentric cylindrical layers of silicon detectors, comprising two layers each of Silicon Pixel Detector (SPD), Silicon Drift Detector (SDD), and Silicon Strip Detector (SSD). The ITS covers the pseudorapidity region  $-\eta \leq 0.9$  for interactions occurring within 10 cm from the detector center. The two innermost layers are constructed using Silicon Pixel Detectors (SPD), located at radial distances of 3.9 cm and 7.6 cm from the beam pipe. These layers cover extended pseudorapidity ranges of  $-\eta \leq 2.0$  and  $-\eta \leq 1.4$ , respectively.

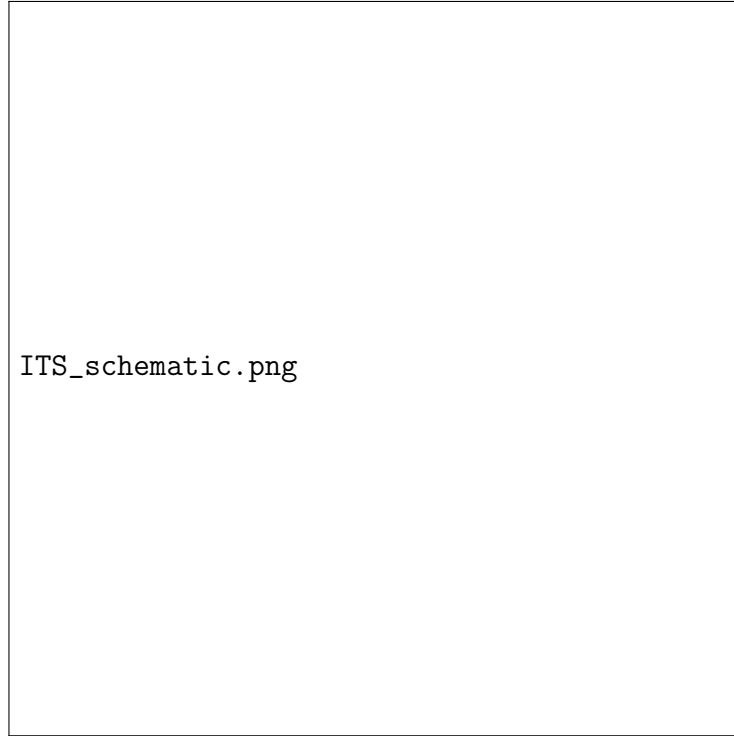


Figure 5.3: Schematic diagram of the Inner Tracking System (ITS) of the ALICE experiment.

They consist of hybrid silicon pixel detectors, totaling  $9.810^6$ , which generate binary signals upon interaction with charged particles, facilitating particle counting. The primary functions of the SPD are to determine the position of the primary vertex with a high resolution, surpassing  $100\text{ }\mu\text{m}$ , to help isolate events coming from pileup, and to contribute to the triggering system due to their fast response. The SPD also ensures the accurate determination of track multiplicity and contributes to achieving an impact-parameter resolution surpassing  $50\text{ }\mu\text{m}$  for tracks with transverse momentum  $p_{\perp} \gtrsim 1.3\text{ GeV}/c$ . The two intermediate layers are the Silicon Drift Detector (SDD), situated at radii of  $15.0\text{ cm}$  and  $23.9\text{ cm}$ , covering  $-\eta \lesssim 0.9$ . The SDD has very good multi-track capability and provides two out of the four measurements of specific  $dE/dx$  employed for PID by the ITS. It provides two-dimensional spatial information ( $r\text{ }\phi$  and  $z$ ) with a spatial resolution of  $35\text{ }\mu\text{m}$  ( $r\text{ }\phi$ ) and  $25\text{ }\mu\text{m}$  ( $z$ ). The SDD determines particle positions using drift time estimation and charge centroid measurement and is structured with a central cathode for precise particle tracking. The two outermost layers employ double-sided Silicon Strip Detectors (SSD), located at radial distances of  $38.0\text{ cm}$  and  $43.0\text{ cm}$ , covering  $-\eta \lesssim 1.0$ . The SSD is essential for the prolongation of tracks from the main tracking detector of ALICE, the Time Projection Chamber (TPC), to the ITS. It provides a spatial resolution of  $20\text{ }\mu\text{m}$  ( $r\text{ }\phi$ ) and  $830\text{ }\mu\text{m}$  ( $z$ ) and  $27\text{ }\mu\text{m}$  ( $r\text{ }\phi$ ) and  $830\text{ }\mu\text{m}$  ( $z$ ) according to the third source, with



a fast readout time of 1  $\mu$ s. Besides connecting tracks, the SSD also provides  $dE/dx$  information, enabling the ITS with the standalone capability to serve as a low-pT particle spectrometer. Each SSD module consists of a 1536-strip double-sided sensor connected to twelve front-end chips that furnish position and energy deposition details. The primary responsibilities of the ITS include:

- Reconstructing the primary vertex of collisions with a high resolution, surpassing 100  $\mu$ m
- Reconstructing the secondary vertices, points of decay for short-lived hadrons
- Particle identification (PID) and tracking of low-momentum particles with momentum below 200 MeV/c.

The ITS can also perform "standalone" tracking that reconstructs charged particles in the low pT region (e.g., pions with pT  $\lesssim$  80 MeV/c) by using exclusively the information from its six planes. The high granularity of ITS allows maintaining the detector occupancy below a safe level. The good resolution of the detector allows to separate primary and secondary vertices from weak decays, hyperons, D and B mesons. The analogue readout in the four outer layers (SDD and SSD) samples the particle energy loss ( $dE/dx$ ) in the material, providing information sufficient to perform PID below 700 MeV/c. [Padhan:2924203] [amsdottorato9036] [Cheng:2908766] [Arata:2922803]

### 5.0.2 Time projection chamber (TPC)

is the main tracking detector of the central barrel. It is specifically designed for measure tracks with transverse momentum range 0.1 GeV/c  $\div$  100 GeV/c and pseudorapidity range  $|\eta| \lesssim 0.9$ . It is positioned at radial distances ranging from 85 to 247 cm from the beam pipe, extending along the beam direction with a total length of 510 cm. It is divided along the beam axis into two equally large drift regions by a central cathode, each having a length of 2.5 m. On the opposite sides of the central electrodes is the readout, which is equipped with multi-wire proportional chambers (MWPC). Each of the 18 readout chambers covers an azimuth of 20°. The grand-total span along the beam direction is of 500 cm. The total volume of TPC ( $\sim 90$  m<sup>3</sup>) can be filled with different gases depending on the running conditions. The perfect candidate are gas with a small radiation length and low multiple scattering rates, usually is filled with a mixture containing different combination of argon, neon, carbon dioxide and sometimes nitrogen. When charged particle traverse the gas ionize him and creating electron-ion pair. These ionization electrons then drift towards sensing electrodes under a uniform electric field, typically achieved by applying a high voltage of around 100 kV between the central electrode and the readout plates. The ionization electrons drift with a speed of approximately 2.7 cm/s, corresponding to a maximum drift time of around

92 ms. This drift process allows for the spatial localization of the ionization event along the particle's trajectory. Additionally, the presence of a uniform magnetic field of 0.5 Tesla along the z-direction causes charged particles to bend in curved paths. It enables precise momentum measurements based on the curvature of the trajectories. The position resolution for the inner/outer radii ranges from 800 to 1100  $\mu\text{m}$  in the transverse plane ( $r, \phi$ ) and from 1100 to 1250  $\mu\text{m}$  along the beam axis ( $z$ ). The total charge collected at the end plates for each track is proportional to the particle energy loss in the gas. This allows a sampling of the  $dE/dx$  and therefore perform PID below 1 GeV/c and above 3 GeV/c. The resolution on the  $dE/dx$  is 5% for isolated tracks (low multiplicity collisions), while the number of particles increase such as Pb–Pb collisions (high multiplicity collisions), the resolution is 7%. This is due to the increased probability to have hits close in space. In addition, the contribution of positive ions to the signal shape increases with the particle occupancy. An other effect is due to the formation of large amount of charged particles that can induce local modifications to the external electric field modifying the drift speed and complicating the reconstruction of the track. It can also be use for identify particle thanks to the measure of  $dE/dx$  as they traverse the gas volume. The specific energy loss can be described by the Bethe-Bloch formula, which depends on the particle species and it momentum, and the properties of the traversed medium, The energy loss can be estimate in the following manner proposed by [Rolandi:2008ujz].

$$f(\beta) = \frac{P_1}{\beta^{P_4}} \left( P_2 - \beta^{P_4} - \ln(P_3) \frac{1}{(\beta\gamma)^{P_5}} \right) \quad (5.1)$$

Where  $\beta$  is the particle velocity in c unit,  $\gamma$  the Lorentz factor,  $P_{1-5}$  free parameter that must be estimate from data.

### 5.0.3 Time Of Flight (TOF)

The Time Of Flight (TOF) detector is a large array of Multi-gap Resistive-Plate Chambers (MRPC), located at 3.7 m and 3.99 m radial distance, respectively, from the interaction point. It is designed to identify charged particle produced in pseudorapidity of  $-\eta \leq 0.9$  and with an intermediate momentum range ( $0.5 \leq p_{\perp} \leq 4$  GeV/c). In addition TOF has been used to provide a trigger specific for cosmic ray and UPC events. The TOF detector has a modular structure divided along the azimuthal direction into 18 super modules, each one segmented into 5 modules along the z axis as visible in Fig ?? . In total there are 1593 Multi-Gap Resistive Plate Chamber (MRPC) strip detectors organized each one divided into two rows of 48 pickup pads, a total of 96 pads per strip and 152 928 readout channels. If a particle ionizes the gas in the detector, an avalanche process will be triggered to generate signal on the readout electrodes. The total signal is the analogue sum of signals from many gaps and the time resolution is about 40 ps with a detector efficiency of

close to 100%. Particle identification is performed by combining the information bring by the linear momentum module ( $p$ ) and track length ( $l$ ) with the measurement of the time of flight ( $t$ ) in TOF. The mass ( $m$ ) corresponding to the one of the detected particle can be obtained.

$$p = m\gamma\beta c \leftrightarrow m = \frac{p\sqrt{1-\beta^2}}{c\beta} = \frac{p\sqrt{\frac{1}{\beta^2}-1}}{c} \quad (5.2)$$

The  $\beta$  parameter can be measured in the following manner

$$\beta = \frac{v}{c} = \frac{l}{c t} \quad (5.3)$$

So

$$m = \frac{p\sqrt{\left(\frac{t}{lc}\right)^2 - 1}}{c} \quad (5.4)$$

The relative uncertainties can be estimated assuming that the variable ar not correlate in the following manner assuming  $c=1$ .

$$\frac{\sigma_m}{m} = \sqrt{\left(\frac{\sigma_p}{p}\right)^2 + \left(\left(\frac{\sigma_t}{t}\right)^2 + \left(\frac{\sigma_l}{l}\right)^2\right) \left(\frac{E}{m}\right)^4} \quad (5.5)$$

The proof is in the appendix. Studying the equation became clear that, at large momenta, the resolution on the track momentum ( $\sigma_p$ ) becomes negligible and the total uncertainty is driven by precision on the timing ( $\sigma_t$ ) and track length ( $\sigma_l$ ). For these reason the TOF detector was designed to achieve a timing resolution better than 90 ps. [Padhan:2924203] [amsdottorato9036] [Cheng:2908766]

## 5.0.4 Central Barrel Detectors

### Transition Radiation Detector (TRD)

The Transition Radiation Detector (TRD) is ositioned between the TPC and TOF detector, it covers a pseudorapidity range of  $-\eta$  i 0.84. It consist in a total of 522 detectors divided into 18 super modules in the azimuthal direction, each super module contains 30 modules arranged in 5 stacks along the beam axis, with each stack further arranged in 6 layers. This configuration results in approximately 1.15 million readout channels. It is principally use for electron identification in hight momentum region ( $p$  i 1 GeV) where discriminating between electrons and pions using traditional  $dE/dx$  techniques becomes challenging and triggering processes within particle collision experiments. When charged the particles try to transverse the detector flows through two media with different dielectric constants and emits transition radiation. The emitted radiation proportional to the Lorentz factor of the particle. Since different particles have different masses and velocities, they emit varying amounts of transition radiation that alow us in the identification. [Padhan:2924203] [amsdottorato9036]

### Photon Spectrometer (PHOS)

The Photon Spectrometer (PHOS) is an electromagnetic calorimeter known for its high spatial and energy resolution. Positioned on the outer region of the TOF detector. PHOS covers a pseudo-rapidity range of  $0.12 < \eta < 0.12$  and provides coverage of 70 in the azimuthal direction using scintillating material called Lead Tungstate ( $PbWO_4$ ). With a dynamic energy range of 0.1 GeV to 100 GeV. Its main goal is to measure QGP temperature, and space-time dimensions, and study deconfinement through jet quenching. [Padhan:2924203] [amsdottorato9036]

### High-Momentum Particle Identification Detector (HMPID)

The High Momentum Particle Identification Detector (HMPID) is a low-acceptance detector. It covers  $\sim 11m^2$  corresponding to 5% of the total central barrel acceptance. Is dedicated to the identification of charged hadrons with  $p_{\perp} > 1$  GeV/c, thus extending the PID capabilities of the ITS, TPC and TOF at high momentum. It covers a pseudorapidity range of  $-0.6 < \eta < 0.6$ . It consists mainly of two parts: the radiator and the photon detector. Comprising seven Ring Imaging Cherenkov (RICH) counters. [Padhan:2924203] [amsdottorato9036]

### Electromagnetic Calorimeter (EMCaL)

The EMCaL is composed of towers of  $6 \times 6 \times 20 \text{ cm}^3$  each one constituted of 76 alternating layers of lead and scintillator (not uniform in contrast to PHOS); it was designed for the measurements of electrons from heavy-flavor hadron decays but not only. It also identifies high-energy particles. In addition it can enhance energy resolution across various momenta, enabling precise measurements of jet quenching. The electromagnetic component of jets, spectra of direct photons and neutral mesons and correlations of those photons with hadrons or jets. It has been completed by the DCal, at the opposite side of the beam. Both calorimeters are trigger detectors and they select collisions when there is a high energy deposition, typically a few GeV. [Padhan:2924203] [Arata:2922803]

## 5.0.5 Forward Detectors

### VZERO detector (V0)

The V0 detector consists of two circular arrays of scintillator counters (named V0A and V0C) one per side with respect to the interaction point. They are positioned asymmetrically on both sides of the interaction point. The V0A covers the pseudorapidity region  $2.8 < \eta < 5.1$  while V0C  $-3.7 < \eta < -1.7$ . They are important both in pp collision and AA collision for the following reason;

- Triggering: The V0 detector provides a minimum bias trigger signal. This is important because help us to detect a broad range of inelastic collision events without introducing significant selection bias.
- Vertex determination: The VZERO detector succeed the rejection of background events generated due to the interaction of beams with residual gas within the beam pipe and with mechanical structures along the beamline. It is possible thanks to the time gap between signals from V0A and V0C.
- Centrality determination: The signal given by the V0 detector is proportional to the number of particles traversing it. So, using the signal aptitude, it can be used for the multiplicity/centrality determination. This information are precious for for understanding the collision geometry and interpreting experimental results accurately.

[Padhan:2924203] [amsdottorato9036]

### T0 Detectors

The T0 detector consists of two arrays, T0A and T0C, of Cherenkov counters placed along the beam pipe on each side of the interaction point, respectively at -72.7 cm and 375 cm. The pseudorapidity coverage are  $4.61 \leq \eta \leq 4.92$  (T0A) and  $-3.28 \leq \eta \leq -2.97$  (T0C). Its primary function is to provide a fast timing signal for the TOF detector, serving as a collision time reference. It can be also use for an independent determination of the vertex position along the beam axis (with a precision of  $\pm 1.5$  cm). [Padhan:2924203] [amsdottorato9036]

### Zero Degree Calorimeter (ZDC)

The Zero Degree Calorimeter (ZDC) consists of four calorimeters, two for protons (brass-quartz proton ZP) and two for neutrons (tungsten-quartz neutron ZN), on each side. located at  $\sim 112.5$  cm away from the Interaction Point, symmetrically in both directions. ZDC measures the energy of spectator nucleons, assisting in centrality estimation and luminosity detection in heavy-ion collisions. By determining collision geometry and overlap regions of colliding nuclei, and estimating the number of participant nucleons.[Padhan:2924203] [amsdottorato9036]

### Muon Spectrometer

The muon spectrometer is located 14 m in the negative beam direction, with a pseudorapidity range of  $4 \leq \eta \leq 2.5$  and the resonances can be detected down to zero transverse momentum. It help to studies the complete spectrum of heavy quarkonia via their decay in the  $\mu^+\mu^-$  channel. It is made of carbon and concrete in order to limit the multiple scattering and the energy loss of

the muons. The inner beam shield protects the chambers from background originating from particles at small angles. It is made of tungsten, lead and stainless steel to minimize the background arising from primary particles emitted in the collision and from their showers produced in the beam pipe and in the shield itself. The 4 planes of RPCs (Resistive Plate Chambers) arranged in 2 stations and positioned behind a passive muon filter provide the transverse momentum of each  $\mu$ . The spatial resolution should be better than 1 cm. Special front-end electronics have been designed to obtain the time resolution of 2 ns necessary for the identification of the bunch crossing. The dipole magnet is positioned at about 7 m from the interaction providing a magnetic field nominally of  $B = 0.7$  T but can be changed by the requirements on the mass resolution. [Padhan:2924203] [Alicemuonspectrometer]

### 5.0.6 Track and vertex reconstruction

The purpose of tracking algorithms [Cheng:2908766] is to use the cluster information transforming them into track information, obtaining the best possible approximation of the real trajectory of the particles crossing the detector. process that uses the Kalman filter algorithm to accurately determine the trajectory of particles as they pass through the detector layers. The tracking procedure starts with the clusterization step. Starting from the collected raw data, from each detector, the data cluster are produced. The cluster correspond to groups of hits produced by a single particle interaction with a detector element and contain his positions, signal amplitude, signal times, and their associated errors. The clusterization is performed separately for each detector. The reconstruction of the primary vertex is an essential step, as it is referred to the interaction point. Usually, each collision event only involves one primary interaction point, and numerous tracks traverse the detectors. In this ambitious the information provided by the SPD detector plays a crucial role in establishing a preliminary interaction vertex. This is the space point that minimises the distance among the tracklets, which are the track segments reconstructed by associating pairs of clusters in the two SPD layers. So is possible to localize the vertex searching the point where most of the tracklets converge. In high multiplicity events the algorithm is repeated several times, discarding at each iteration those clusters which contributed to already found vertices. The tracking algorithm can be separated into two steps: the track finding and the track fitting. For the track finding, two methods are used. The first one is called Linear Track Finder (LTF) and it looks for cluster position aligned along a straight line. However the magnetic field curve the trajectory of charged particle but the deviation can be neglected at least at high  $p_{\perp}$  hence supporting the choice of a LTF for such tracks. For help in these work a radial tolerance  $R_{cut}$  is given, a graphical resume is visible in Fig 5.4 . If a track had been recognized in the previous step the correspondent cluster are removed from the list of available clusters considered in the further

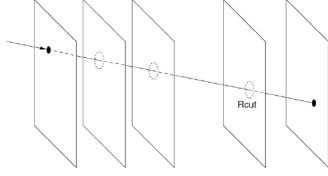


Figure 5.4: The figure show Linear Track Finder schematic using the RCut parameter [CERN-LHCC-2015-001]

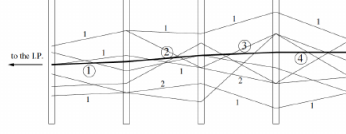


Figure 5.5: The figure show how the Cellular Automaton method works [CERN-LHCC-2015-001]

steps. The next step consist on a Cellular Automaton (CA) approach particularly suited for low-momentum tracks, sensitive to multiple scatterings. It is based on a propagation and joining of “segments”. A segment is a portion of line connecting two clusters from two consecutive disks: So starting from a given segment, considered as the first, the algorithm search the further one towards imposing track continuity conditions. The strategiest is visible in Fig 5.5. Tracks are only accepted if they have at least 20 associated clusters (out of a possible 159) and have missed fewer than 50% of the expected clusters. Only after that the track candidates are found a track fitting algorithm is applied in order to extract the kinematic parameters of each track. It is able to determine the spatial and momentum coordinates considering material effects, updates the parameters based on measurement. The process is repeated for each track cluster [Herrmann:2920632].

The efficiency of the track reconstruction process is influenced by the transverse momentum of the tracks. Efficiency drops below  $p_{\perp} \downarrow 0.5$  GeV/c, as visible in Fig 5.6 due to energy loss in the detector material, while higher  $p_{\perp}$  tracks, which are typically straighter, may encounter reduced efficiency in areas where clusters are lost due to dead zones between readout sectors. [Padhan:2924203].

More specifically for primary vertex finding the most useful instrument is the SPD. It is ideal for fast vertex measurements as it provides a quick response, also because is closest to the interaction point, and has excellent transverse plane resolution due to its high granularity. The resolution of the SPD Vertex is of  $10 \mu\text{m}$  in Pb–Pb collisions and  $150 \mu\text{m}$  in pp collisions at  $\sqrt{s_{NN}} = 7$  TeV. In ALICE, three primary algorithms are used for vertex reconstruction

- VertexerSPDz: Provides the measurement of the z-coordinate of the interaction point using the SPD. It calculates the z-coordinate from tracklets correlations in the SPD layers and iteratively refines the estimate by focusing on the peak of the z-distribution.
- VertexerSPD3D: Offers a three-dimensional measurement of the primary vertex using the SPD tracklets. To perform the task it minimize the distances among tracklets.

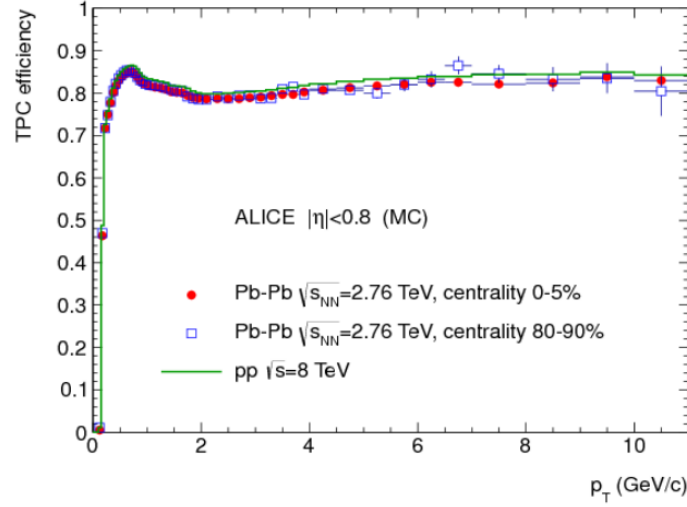


Figure 5.6: The figure show track finding efficiency for primary particles in different types of collision [ALICE:2014sbx]

- VertexerTracks: Provides a three-dimensional measurement of the primary vertex using reconstructed tracks. Where the final vertex position and its covariance matrix are obtained through a fitting process.

[Padhan:2924203] Once the tracks and the interaction vertex have been found in the course of event reconstruction, a search for photon conversions and secondary vertices from particle decays is performed. Instead the hadronic interaction vertices are found at the analysis level by identifying groups of two or more tracks originating from a common secondary vertex with precises restriction in the invariant mass of the pair. In ALICE, secondary vertex reconstruction begins by selecting tracks with Distance of Closest Approach DCA greater than 0.5 mm in pp collisions or 1 mm in Pb–Pb collisions. A graphical resume is visible in Fig 5.7. For each pair of selected tracks with opposite charges, known as  $V^0$  candidates, are then subjected to further selection criteria:

1. The distance between the two tracks at their PCA is requested to be less than 1.5 cm
2. The PCA is requested to be closer to the interaction vertex than the innermost hit of either of the two tracks.
3. The cosine of the angle between the total momentum vector of the pair and the line connecting the primary and secondary vertices must be greater than 0.9

For  $V^0$  candidates with a momentum below 1.5 GeV/c the cut are relaxed. The reconstruction of more complex secondary vertices is performed later, at



the analysis stage. For the study of heavy-flavor decays close to the interaction point, the secondary vertex is searched starting from point that satisfied other different topological condition. [ALICE:2014sbx]

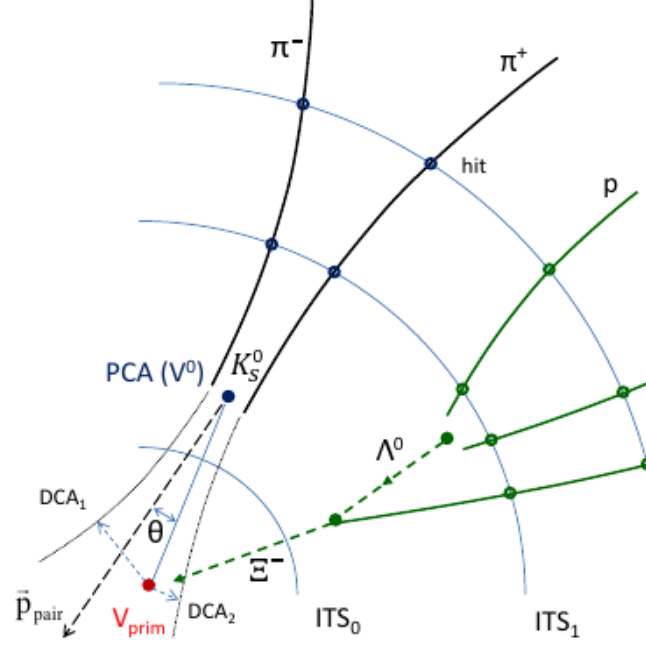


Figure 5.7: The figure show the secondary vertices reconstruction procedure for different particles. Using long lives particles are detected and neutral vertices are reconstructed by back-propagating charged particles. The total reconstructed momentum and its orientation constitute useful quantities for background rejection. [ALICE:2014sbx]

## A Appendix A

We start with the proof that  $dy p_{\perp} dp_{\perp} d\phi_p = dy m_{\perp} dm_{\perp} d\phi_p$ , in fact  $m_{\perp} = \sqrt{m^2 + p_{\perp}^2}$  so  $\frac{dm_{\perp}}{dp_{\perp}} = \frac{p_{\perp}}{\sqrt{m^2 + p_{\perp}^2}} = \frac{p_{\perp}}{m_{\perp}}$  and the result follow immediately.

For the other equation starting from 3.8 and inserting 3.2 one get

$$\begin{aligned}
 \frac{dN_i}{dy m_\perp dm_\perp d\phi_p} &= \frac{g_i}{(2\pi)^3} \sum_{n=1}^{\infty} (\pm)^n \int d^2 r_\perp \tau_f e^{n\mu_i/T} e^{n\gamma_\perp v_\perp \cdot \vec{p}_\perp} \\
 &\quad \int_{-\infty}^{+\infty} d\eta (m_\perp \cosh(y - \eta) - \vec{p}_\perp \cdot \nabla_\perp \tau_f) e^{-n\gamma_\perp m_\perp \cosh(y - \eta)/T} \\
 &= \frac{g_i}{(2\pi)^3} \sum_{n=1}^{\infty} (\pm)^n \int d^2 r_\perp \tau_f e^{n\mu_i/T} e^{n\gamma_\perp v_\perp \cdot \vec{p}_\perp} \\
 &\quad \left( m_\perp K_1 \left( nm_\perp \frac{\gamma_\perp(\vec{r}_\perp)}{T(\vec{r}_\perp)} \right) - \vec{p}_\perp \cdot \nabla_\perp \tau_f K_0 \left( nm_\perp \frac{\gamma_\perp(\vec{r}_\perp)}{T(\vec{r}_\perp)} \right) \right)
 \end{aligned} \tag{6}$$

Where the modified Bessel function enters the game. The azimuthal integral can thus be done analytically

$$\begin{aligned}
 \frac{dN_i}{dy m_\perp dm_\perp} &= \frac{g_i}{\pi^2} \sum_{n=1}^{\infty} (\pm)^n \int_0^\infty r_\perp dr_\perp \tau_f e^{n\mu_i/T} \\
 &\quad \left( m_\perp K_1 \left( nm_\perp \frac{\gamma_\perp(\vec{r}_\perp)}{T(\vec{r}_\perp)} \right) I_0 \left( n \frac{p_\perp v_\perp \gamma_\perp}{T} \right) \right. \\
 &\quad \left. - p_\perp \frac{\partial \tau_f}{\partial r_\perp} K_0 \left( nm_\perp \frac{\gamma_\perp(\vec{r}_\perp)}{T(\vec{r}_\perp)} \right) I_1 \left( n \frac{p_\perp v_\perp \gamma_\perp}{T} \right) \right)
 \end{aligned} \tag{7}$$

And finally, defining  $v_\perp = \tanh(\rho)$  and  $\eta(\vec{r}_\perp) = \tau_f e^{n\mu_i/T}$ , one obtains

$$\begin{aligned}
 \frac{dN_i}{dy m_\perp dm_\perp d\phi_p} &= \frac{g_i}{\pi} \int_0^\infty r_\perp dr_\perp n_i(r_\perp) \left[ m_\perp K_1 \left( \frac{m_\perp \cosh(\rho(r_\perp))}{T(r_\perp)} \right) \right. \\
 &\quad I_0 \left( \frac{p_\perp \sinh(\rho(r_\perp))}{T(r_\perp)} \right) - p_\perp \frac{\partial \tau_f}{\partial r_\perp} K_0 \left( \frac{m_\perp \cosh(\rho(r_\perp))}{T(r_\perp)} \right) \\
 &\quad \left. I_1 \left( \frac{p_\perp \sinh(\rho(r_\perp))}{T(r_\perp)} \right) \right]
 \end{aligned} \tag{8}$$

## B Appendice B

Under free-streaming the phase space distribution evolves as

$$f(\vec{r}, \vec{p}, t) = f\left(\vec{r} - \frac{\vec{p}}{E}(t - t_0), \vec{p}, t\right) \tag{9}$$

Using a Gaussian parametrization for the initial phase-space distribution of produced secondary particles

$$f(\vec{r}, \vec{p}, \tau) = e^{-\frac{x^2}{2R_x^2} - \frac{y^2}{2R_y^2} - \frac{p_x^2 + p_y^2}{2(\Delta\tau)^2}} \tag{10}$$

where  $\Delta t$  so writing the Eq 3.17 in integral form.

$$\epsilon_x = \frac{\int d^2 r r^2 \cos(2\psi_r \int d^3 p f(\vec{r}, \vec{p}, \tau))}{\int d^2 r r^2 \int d^3 p f(\vec{r}, \vec{p}, \tau)} \approx \frac{R_x^2 + R_y^2}{R_x^2 + R_y^2 + 2(c\Delta\tau)^2} \quad (11)$$

One get

$$\frac{\epsilon_x(t_0 + \Delta T)}{\epsilon_x(\tau_0)} = \left[ 1 + \frac{(c\Delta\tau)^2}{\langle \vec{r}^2 \rangle_{\tau_0}} \right]^{-1} \quad (12)$$

## C Appendice C

For get the gran canonical partition function starting from Eq 3.24 visible below.

$$\ln Z_i(T, V, \mu_i) = \frac{\Delta V g_i}{2\pi^2 \hbar^3} \int_0^\infty \theta_i p^2 dp \ln(1 + \theta_i e^{\beta(\mu_i - E)}) \quad (13)$$

replacing the logarithm with taylor expansion under the assumption that  $e^{\beta(\mu_i - E)} < 1 \rightarrow \mu_i < E$  and using  $\lambda_i = e^{\beta\mu_i}$  it's possible to rewrite 3.2.

$$\ln Z_i(T, V, \mu_i) = \frac{\Delta V g_i}{2\pi^2 \hbar^3} \sum_K \frac{(\theta \lambda_i)^k}{k} \int_0^\infty p^2 dp e^{-k\beta E} \quad (14)$$

integrating by part

$$\ln Z_i(T, V, \mu_i) = \frac{\Delta V g_i}{2\pi^2 \hbar^3} \sum_K \frac{(\theta \lambda_i)^k}{k} \left[ \frac{p^3 e^{-k\beta E}}{3} \Big|_0^\infty + \int_0^\infty dp \frac{p^3}{3} \frac{\beta e^{-k\beta E}}{3} \frac{dE}{dp} \right] \quad (15)$$

The first integrand vanish.

$$\frac{dE}{dp} = \frac{d}{dp}(\sqrt{p^2 + m_i^2}) = \frac{p}{\sqrt{p^2 + m_i^2}} = \frac{p}{E} \quad (16)$$

so

$$\ln Z_i(T, V, \mu_i) = \frac{\Delta V g_i}{2\pi^2 \hbar^3} \sum_K \frac{(\theta \lambda_i)^k}{k} \int_0^\infty dp \frac{p^3}{3} \frac{\beta e^{-k\beta E}}{3} \frac{E}{p} \quad (17)$$

introducing  $x = k\beta E$ ,  $w_i = k\beta m_i$  and  $y_i = x/w_i$

$$\ln Z_i(T, V, \mu_i) = \frac{\Delta V g_i}{2\pi^2 \hbar^3} \sum_K \frac{(\theta \lambda_i)^k}{k} \int_0^\infty dE \frac{p^3 k \beta e^{-k\beta}}{3} \quad (18)$$

$$\ln Z_i(T, V, \mu_i) = \frac{\Delta V g_i}{2\pi^2 \hbar^3} \sum_K \frac{(\theta \lambda_i)^k}{k} \int_0^\infty dE \frac{(E^2 - m_i^2)^{3/2} k \beta e^{-k\beta}}{3} \quad (19)$$

$$\ln Z_i(T, V, \mu_i) = \frac{\Delta V g_i m_i^2}{2\pi^2 \hbar^3 \beta} \sum_K \frac{(\theta \lambda_i)^k}{k^2} \int_0^\infty dE \frac{(x^2 - w_i^2)^{3/2}}{3w_i^2} e^{-x} \quad (20)$$

$$\ln Z_i(T, V, \mu_i) = \frac{\Delta V g_i m_i^2}{6\pi^2 \hbar^3 \beta} \sum_K \frac{(\theta \lambda_i)^k w_i}{k^2} \int_0^\infty dE \left( \frac{x^2}{w_i^2} - 1 \right)^{3/2} e^{-x} \quad (21)$$

$$\ln Z_i(T, V, \mu_i) = \frac{\Delta V g_i m_i^2}{6\pi^2 \hbar^3 \beta} \sum_K \frac{(\theta \lambda_i)^k w_i}{k^2} \int_0^\infty dE w_i (y^2 - 1)^{3/2} e^{-w_i y} \quad (22)$$

introducing the modified Bessel function

$$k_2(q) = \frac{q^2}{3} \int_0^\infty dy (y^2 - 1)^{3/2} e^{-qy} \quad (23)$$

we finally obtain

$$\ln Z_i(T, V, \mu_i) = \frac{\Delta V g_i}{2\pi^2 \hbar^3 \beta} \sum_K \frac{(\theta_i e^{\beta \mu_i})^k}{k^2} m_i^2 K_2(k\beta m_i) \quad (24)$$